國 立 交 通 大 學

光電工程研究所

碩 士 論 文

在鈦酸鉛及氧化鐵鈷的多重鐵性系統中研究受應力影響之介面聲子與鐵磁特性

Stress-Dependent Interfacial Phonon and Ferromagnetic Properties in PbTiO$_3$-CoFe$_2$O$_4$ Multiferroic System

研 究 生：蔡智雅

指導教授：謝文峰　教授

中 華 民 國 九 十 八 年 六 月

在鈦酸鉛及氧化鐵鈷的多重鐵性系統中研究受應力影響之介面聲子與鐵磁特性

Stress-Dependent Interfacial Phonon and Ferromagnetic Properties in PbTiO$_3$-CoFe$_2$O$_4$ Multiferroic System

研 究 生：蔡智雅　　　　　　　　　Student：Chih-Ya Tsai

指導教授：謝文峰 教授　　　　　　Advisor：Wen-Feng Hsieh

國 立 交 通 大 學

光 電 工 程 研 究 所

碩 士 論 文

A Thesis
Submitted to Institute of Electro-optical Engineering
College of Electrical Engineering and Computer Science
National Chiao Tung University
in Partial Fulfillment of the Requirements
for the Degree of
Master
in
Electro-optical Engineering
June 2009
Hsinchu, Taiwan, Republic of China

中 華 民 國 九 十 八 年 六 月

在鈦酸鉛及氧化鐵鈷多重鐵性系統中研究跟應力相關的介面聲子及鐵磁特性

研究生：蔡智雅　　　　　　　　　　　　　　指導教授：謝文峰　教授

國立交通大學光電工程研究所

摘要

在此篇論文中，我們藉由顯微拉曼光譜研究在以鈦酸鉛為基質而含有三種不同幾何結構的氧化鐵鈷之多重複合鐵性材料中之介面聲子及鐵磁特性與應力的相關性。多重複合鐵性材料在介面上的聲子能量和鐵磁特性跟應力的關係不只源自於氧化鐵鈷跟鈦酸鉛基底的晶格大小差異，也跟他們在介面上的化學鍵結強度相關。其中，以 disk-3 型態的多重複合鐵性材料，即為自組裝的盤狀氧化鐵鈷鑲嵌於鈦酸鉛基質中，顯現出在鐵磁相與鐵電相間有最強的彈性交互作用力。相較於氧化鐵鈷與鈦酸鉛的層狀結構(2-2)或氧化鐵鈷粒子懸浮於鈦酸鉛中的結構(0-3)而言，disk-3 的氧化鐵鈷在磁滯曲線上有較低且較不對稱的矯頑場及難以被飽和的磁化量，這些皆與鈦酸鉛在拉曼光譜中的 A_1(2TO)和 A_1(3TO)模態有較多的紅位移相吻合。

Stress-dependent interfacial phonon and ferromagnetic properties in PbTiO$_3$-CoFe$_2$O$_4$ multiferroic system

Student: Chih-Ya Tsai

Advisor: Prof. Wen-Feng Hsieh

Institute of Electro-optical Engineering

National Chaio Tung University

Abstract

Abstract

We report on the relationship between local behavior of interfacial phonon and ferromagnetic properties in three multiferroics consisting of different geometric shapes of ferromagnetic CoFe$_2$O$_4$ (CFO) embedded in ferroelectrics PbTiO$_3$ (PTO) studied by micro-Raman spectroscopy. The energy of interfacial phonon and ferromagnetic properties depend on stress due to not only the lattice misfit but also the degree of chemical bonding at the interface between CoFe$_2$O$_4$ and PbTiO$_3$ matrix. In one dimension (1D) embedded in 3D or disk-3 type structure, the self-assembled CFO disks embedded in a PTO matrix, illustrates strong elastic interactions between the two phases. The larger nonsymmetrical coercivity Hc

and the absence of saturation magnetization Ms of CFO matche with the more Raman shift of

A_1(2TO) and A_1(3TO) modes of PTO found in the disk-3 type than the other types of CFO and

PTO multilayered structure and the CFO particles embedded in PTO matrix.

Content

Chapter 1 Introduction

Chapter 2 Theoretical Background

Chapter 3 Experimental Details

Chapter 4 Results and Discussion

Chapter 5 Conclusion

List of Figures

List of Tables

Chapter 1 Introduction

1.1 A Review of Ferroelectric Materials

1.1.1 Ferroelectricity and Piezoelectricity

Ferroelectricity is a phenomenon that materials exhibit a spontaneous polarization on cooling below the Curie temperature (T_C).   It was discovered in the barium titanate ($BaTiO_3$), one of the pervoskite structure materials, in 1940s.   The occurrence of electric diploes below T_c in the perovskite-structure crystals is due to the shift of center positive charge along c-axis of the crystal.   The plot of polarization versus electric field for the ferroelectric state shows a hysteresis loop.   Owing to the hysteresis, ferroelectric materials have long been used in bulk form in a variety of fields.   Today, ferroelectric materials are deposited in thin films and they are essential materials for a variety of devices such as ferroelectric random access memory (FRAM), infrared pyroelectric sensors, transistors, microwave electronics, electro-optic modulators and other integrated devices.   Among many classes of ferroelectric materials, the perovskite compounds such as the lead lanthanum titanate (PLT) [1], lead zirconate titanate (PZT) [2], lead titanate (PT) [3], and barium titanate (BT) [4] have been the most intensively investigated.
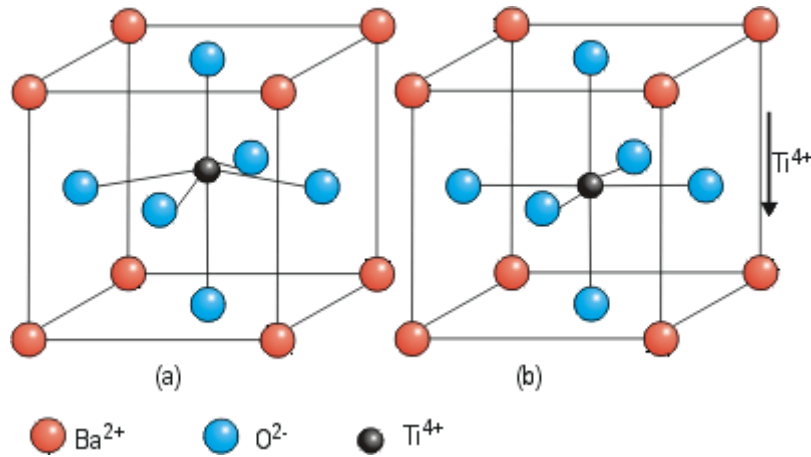
Figure 1-1 Structures of perovskites: (a) tetragonal structure below the Curie temperature
and (b) cubic structure above the Curie temperature.

All crystals in a ferroelectric state are also piezoelectric; a stress Z applied to the crystal

will change the electric polarization. Similarly, an electric field E applied to the crystal will

cause it to become strained. In schematic one-dimensional notation, the piezoelectric

equations are

$$P = Zd + E\chi; \quad e = Zs + Ed,$$

where P is the polarization, Z the stress, d the piezoelectric strain constant, E the electric field,

χ the dielectric susceptibility, e the elastic strain, and s the elastic compliance constant. A

crystal may be piezoelectric without being ferroelectric; a schematic example of such a

structure is given in Fig. 1-3. Quartz is piezoelectric, but not ferroelectric; barium titanate is

both. For order of magnitude, in quartz d $\equiv 10^{-7}$ cm/statvolt and in barium titanate d $\equiv$

10^{-5} cm/statvolt. The general definition of the piezoelectric strain constants is

$$d_{ik} = \left(\frac{\partial e_k}{\partial E_i}\right)_z$$
,

where $i \equiv x, y, z$ and $k \equiv xx, yy, zz, yz, zx, xy$. To convert to cm/stat-V from the values of

d_{ik} given in m/V, just multiply by a factor of 3×10^4[6]. The effect finds useful applications

such as the production and detection of sound, generation of high voltages, electronic

frequency generation, microbalances, and ultra fine focusing of optical assemblies. It is also

the basis of a number of scientific instrumental techniques with atomic resolution, the

scanning probe microscopes such as scanning tunneling microscopy (STM), atomic force

microscope (AFM), scanning near-field optical microscopy (SNOM) etc.
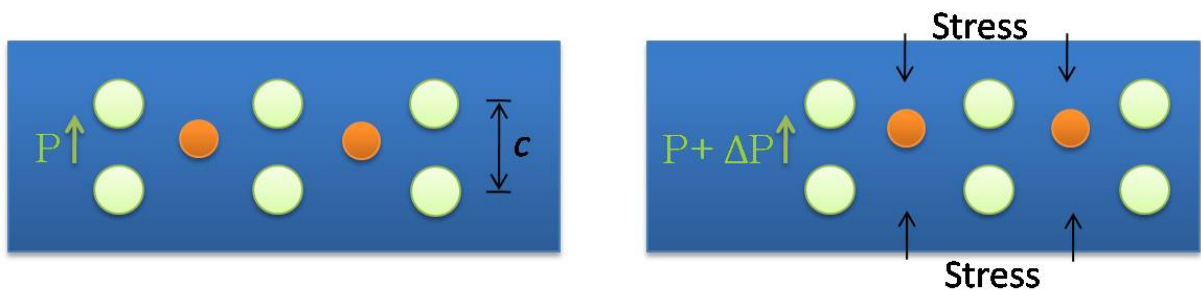
Figure 1-2 Unstressed (a) and stressed (b) ferroelectric crystal. The stress changes the
polarization by $\triangle$P, the induced piezoelectric polarization.
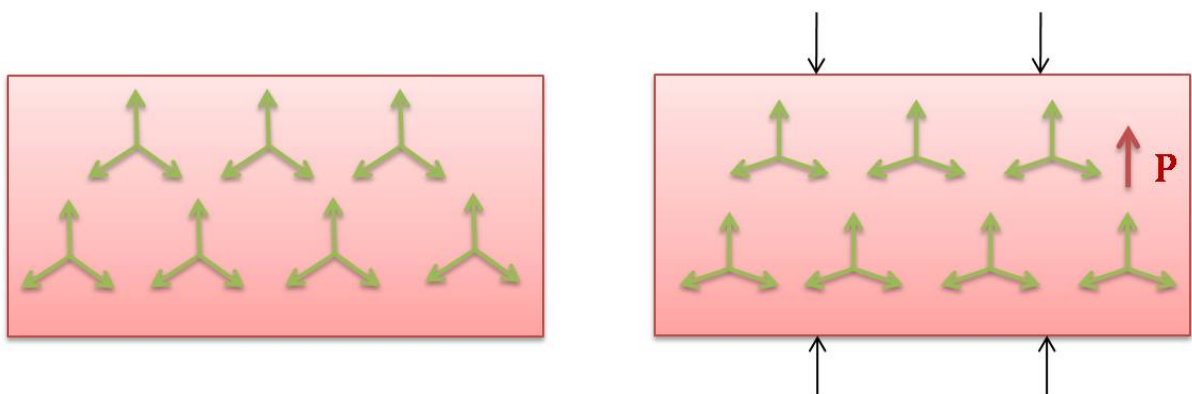
Figure 1-3 Ferroelectricity of threefold symmetry structure. (a) The unstressed crystal $A^{+}_3B^{3-}$
has a threefold symmetry axis with B^{3-} ion at each vertex. The sum of the three dipole
moments at each vertex is zero. (b) The crystal when stressed develops a polarization and the
sum of dipole moments at each vertex is no longer zero.

1.2 A Review of Ferromagnetic Materials

1.2.1 Magnetism

The origin of magnetism lies in the orbital and spin motions of electrons and how the electrons interact with one another. The best way to introduce the different types of magnetism is to describe a net magnetization corresponding to the alignment of magnetic moments under an applied magnetic field [5].

"Ferromagnetism" describes the property only when all magnetic moments are strongly coupled and add a positive contribution to the net magnetization after setting the external magnetic field to zero. If some of the magnetic moments are partially anti-aligned and add a net magnetization, then the material is "ferrimagnetic". If the identical moments anti-align completely so as to have zero net magnetization, despite the magnetic ordering, then it is antiferromagnetism. All of the above alignment effects only occur at temperatures below a certain critical temperature, called the Curie temperature (for ferromagnets and ferrimagnets) or the Neel temperature (for antiferromagnets). Paramagnetism happens when the magnetic moments are very loosely coupled so that thermal energy randomizes their orientation. All atoms, including magnetic ones, exhibit diamagnetism, which is a small current induced to oppose the external magnetic field by Lenz's law [5].

Ferromagnet   Antiferromagnet   Ferrimagnet

Figure 1-4 Ferromagnetism: (a) Ferromagnetic materials exists a strong coupling between magnetic atoms and the spins align in the same direction even at zero field.   (b) An opposite coupled spins in antiferromagnetic materials (NiO, CoO) makes the net moment is zero.   (c) Ferrimagnetism such as TbFe and Fe_3O_4 possesses unequal magnetic moments and hence nonzero moments.

1.2.2 Ferromagnetism and Hysteresis Loop

Ferromagnetic (ferrimagnetic) materials have a large and positive susceptibility to an external magnetic field.   They exhibit a strong attraction to magnetic fields and are able to retain their magnetic properties after the external field has been removed.   When the individual moments of the atoms are aligned with one another, a uniform magnetized region within a material forms and is called as domain.   In these domains, large numbers of atom's moments (10^{12} to 10^{15}) are aligned parallel so that the magnetic force within the domain is strong.   When a ferromagnetic material is in the demagnetized state, the domains are nearly randomly organized and the net magnetic field for the part as a whole is zero.   When a magnetizing force is applied, the domains become aligned to produce a strong magnetic field within the part.   Iron, nickel, and cobalt are examples of ferromagnetic materials [6].

Figure 1-5 is a typical magnetization curve for ferromagnetic materials [6]. Magnetization (emu/cc) is plotted as a function of magnetic field intensity (Oe).   In materials

5

science, the coercivity, also called the coercive field, of a ferromagnetic material is the intensity of the applied magnetic field required to reduce the magnetization of that material to zero after the magnetization of the sample has been driven to saturation. Coercivity is usually measured in oersted or ampere/meter units and is denoted H_C. The saturation magnetization (Ms) means the magnetization M stays constant even when the applied field is increasing continuously. After saturation, the external field is set to zero and the residual magnetization was called Remnant magnetization (Mr) [5].
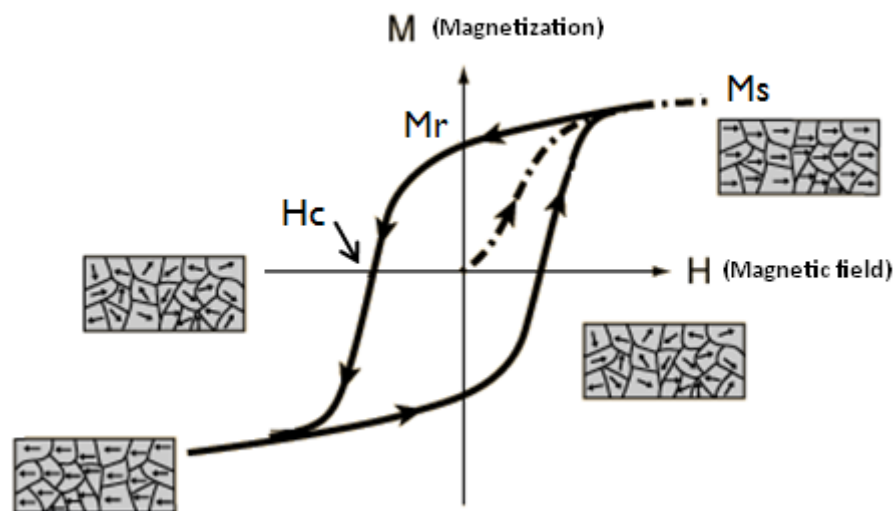
Figure 1-5 The Magnetization curves and hysteresis loops for ferromagnetic materials.

1.2.3 Magnetostriction

Magnetostriction is the name given to the changes of size and shape of structure which accompany the magnetization of a ferromagnetic. The phenomenon was discovered by Joule J.P. and published in Philosophical Magazine in 1847 [7]. Nearly all ferromagnetic

materials exhibit a change in shape resulting from magnetization change. The fact that magnetization causes mechanical strain implies that mechanical stress will affect the magnetization. It is this inverse effect that gives magnetostriction phenomena, the chief importance, for causing external or internal mechanical stresses to have a profound influence on the magnetic properties of a body [6].

In describing anisotropic magnetostriction in a material one can refer to its magnetostrictive constants, λ_s, the strains produced at magnetic saturation, or to its magnetoelastic coupling coefficients, B_{ij}, the magnetic stresses causing λ_s [6]. In most common materials, nickel, iron, and cobalt, the change in length is on the order of 10 parts per million. The highest room temperature magnetostriction of a pure element is that of Co which saturates at 60 microstrain. Fortunately, by alloying elements one can achieve "giant" magnetostriction under relatively small fields. The engineering era of magnetostrictive materials began with the discovery of giant (1000's of ppm) magnetostriction in rare earth alloys during the 1960's by A.E. Clark and others [8]. The culmination of research into a engineering alloy incorporating rare earth materials was Terfenol-D, a specially formulated alloy of Terbium, Dysprosium, and Iron that exhibits large magnetostriction at room temperature and relatively small applied fields [9].

Table 1-1 Magnetostriction Constrants λ_{100} and λ_{111} ($\times 10^6$) at 4.2K and Room Temperature for several materials [5]

	T = 4.2K		Room Temperature		
	$\lambda_{100}(\lambda^{\gamma,2})$	$\lambda_{111}(\lambda^{\varepsilon,2})$	$\lambda_{100}(\lambda^{\gamma,2})$	$\lambda_{111}(\lambda^{\varepsilon,2})$	Polycrystal λ_s
3d Metals					
BCC-Fe	26	-30	21	-21	-7
HCP-Co[u]	(-150)	(45)	(-140)	(50)	(-62)
FCC-Ni	-60	-35	-46	-24	-34
BCC-FeCo	--	--	140	30	--
a-$Fe_{80}B_{20}$	48 (isotropic)	--	--	--	+32
a-$Fe_{40}Ni_{40}B_{20}$	+20	--	--	--	+14
4f Metal / Alloys					
Gd[u]	(-175)	(105)	(-10)	0	--
Tb[u]	--	(8700)	--	(30)	--
$TbFe_2$	--	4400	-	2600	1753
$Tb_{0.3}Dy_{0.7}Fe_2$	--	--	--	1600	1200
Spinel Ferrits					
Fe_3O_4	0	50	-15	56	+40
$MnFe_2O_4$	--	--	(-54)	(10)	--
$CoFe_2O_4$	--	--	-670	120	-110
Garnets					
YIG	-0.6	-2.5	-1.4	-1.6	-2
Hard Magnets					
$Fe_{1.4}Nd_2B$[u]	--	--	--	--	--
$BaO \bullet 6Fe_3O_4$[u]	--	--	(13)	--	--

1.3 Multiferroic Materials

1.3.1 Origin of Multiferroics

Materials in which ferromagnetism and ferroelectricity occur simultaneously in the same composite and allow coupling between the two order-parameters are known as multiferroics [10]. As a consequence, they have a spontaneous magnetization that can be switched by an applied electric field and a spontaneous electrical polarization that can be switched by an applied magnetic field. This is the famous magnetoelectric effect (ME effect) [11]. The figure below shows the definitions of multiferroics and magnetoelectrics. Although initially with different meanings, they have been widely used and interchangeable now.
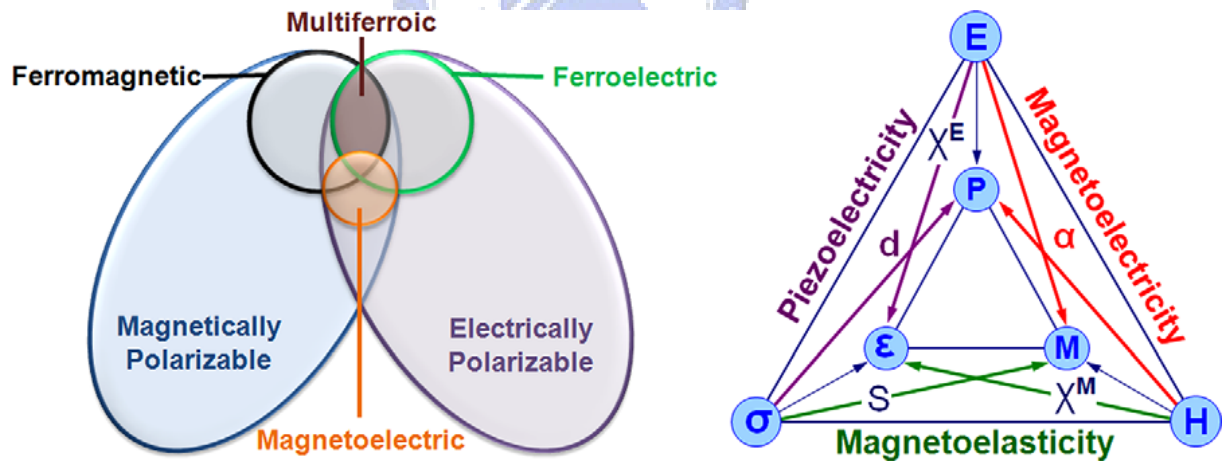
Figure 1-6 Schematic illustration of multiferroics. (a) Relationship between multiferroic and magnetoelectric materials illustrates the requirements to achieve both in a material. (b) Schematic illustrating different types of coupling present in materials. Much attention has been given to materials where electric and magnetic order are coupled known as magnetoelectric materials.

Hitherto, there have been very few multiferroics existing in nature or synthesized in the

laboratory. The first discovered multiferroic material was nickel iodine boracite, ($Ni_3B_2O_{13}I$) [12]. This discovery was followed by the synthesis of several multiferroic boracites compounds, all of which have complex structures with many atoms per formula unit and more than one formula unit per unit cell. The large number of inter-ionic interactions in these materials prevented isolation of the essential factors causing multiferroicity and the nature of the coupling between the magnetic and electric polarization, and structural order parameters. The search for other multiferroics began in Russia as early as the 1950s, with the replacement of some of the B cations contenting zero d-orbital electrons in ferroelectric perovskite oxides by magnetic d^n cations [13]. The first synthetic multiferroic material, $(1-x)PbFe_{0.66}W_{0.33}O_3 - xPbMg_{0.5}W_{0.5}O_3$ [14], was produced at the beginning of the 1960s. In this case, Mg^{2+} and W^{6+} ions were diamagnetic and caused ferroelectricity whereas d^5 Fe^{3+} ions are responsible for the magnetic ordering. As a result of the dilution of the magnetic ions, these materials all have rather low Curie or Neel temperatures.

In the past few years, there has been renewed interest in studying the perovskite-based multiferroic materials, such as rare earth manganates $TbMn_2O_5$, $YMnO_3$, $BiMnO_3$, which have higher Curie temperatures and large magnetoelectric effects. Furthermore, recently efforts have been made to synthesize the new multiferroic in the form of thin film, by employing ferroelectric and ferromagnetic compounds to make a nanocomposite, a superlattice, or a multilayer structure [18].

However the single-phase ME materials show weak ME coupling due to the basic problem that the electric configurations favoring magnetization are antagonistic to those that favor polarization [19]. Van Suchtelen proposed the concept of a product property in two-phase composite materials in 1972, arising from an elastic coupling between two phases of different properties. The ME effect in a composite material having one magnetostrictive and one piezoelectric phase is one such product tensor property. Scientists in Philips Laboratory experimentally found that large ME effect could be produced in such composites [7]. The ME effect obtained in this way can reach about hundred times larger than that in single-phase multiferroic one.

A milestone in the development of ME bulk composites was the appearance of one containing giant magnetostrictive rare-earth-iron alloy $Tb_{1-x}Dy_xFe_2$ (Terfenol-D) in 2001. The Terfenol-D/PZT and Terfenol-D/PVDF composites have been experimentally found to exhibit a giant ME effect [20]. In 2004, Zheng et al. reported a pioneering experiment on nanostructured films of the $BaTiO_3$-$CoFe_2O_4$ system with 1-3 connectivity schemes [11]. In the last two years, a series of experimental and theoretical work on such multiferroic oxides has been reported. Such multiferroic nanostructures have become the topic of the day in the multiferroic composites field, and they promise potential applications of ME composites in microelectronic devices.

1.3.2 Classification of multiferroic materials

Magnetoelectric materials with coexistence of at least two ferroic orders are divided into single-phase and multiphase multiferroics by their composition and phase connectivity.

1.3.2.1 Single-phase multiferroics

Single-phase multiferroics contains only one component but posses both ferroelectric and ferromagnetic properties. However, there is a contra-indication between the conventional mechanism for cation off-centering in ferroelectrics (which require formally empty d orbitals), and the formation of magnetic moments (which usually results from partially filled d orbitals). This is the main challenge in studying single-phase multiferroics since 1960s. For ferroelectricity and magnetism to coexist in a single phase, the atoms that move off center to form the electric dipole moment should be different from those that carry the magnetic moment. Different mechanisms to single-phase multiferroics were studied and the most common routes were listed [18].

In the magnetic perovskite-structure oxides and related materials, multiferroism is most commonly achieved by making use of the stereochemical activity of the lone pair on the large (A-site) cation to provide the ferroelectricity, while keeping the small (B-site) cation magnetic. This is the mechanism for ferroelectricity in the Bi-based magnetic ferroelectrics, the most widely studied of which is bismuth ferrite, $BiFeO_3$. A second route to multiferroism is provided by "geometrically driven" ferroelectricity, which is compatible with the coexistence of magnetism; the antiferromagnetic ferroelectrics $YMnO_3$ and $BaNiF_4$ fall into this class [21].

To be ferroelectric, a material must be insulating otherwise the mobile charges would screen out the electric polarization. This is a common problem in the case of magnetic ferroelectrics, because magnetic transition metal ions are often able to accommodate a wider range of valence states than their diamagnetic counterparts, leading in turn to non-stoichiometry and hopping conductivity. Clearly many potential combinations of lone pairs and transition metals remain to be explored, but in all cases, the stoichiometry must be carefully controlled so that the transition metal d electrons provide magnetism without also contributing to electronic transport. Therefore, detailed characterization of the domain structure, dynamics for improving magnetoelectric coupling, and reduction of the leakage current density and the coercive field, are critical challenges that need to be addressed before $BiFeO_3$-based films will be candidates for integrated microelectronic devices such as storage elements in non-volatile ferroelectric memories [7].

1.3.2.2 Multiphase multiferroics

Multiphase multiferroics are investigated as an alternative approach using bonded magnetostrictive and piezoelectric materials to overcome the low ME coupling and low-temperature problems of single-phase multiferroics. The classification of multiphase multiferroics is based on the phase connectivity.   They are divided into the following types: As for piezoelectric composites, the ME composites could have various connectivity schemes, but the common connectivity schemes are 0-3–type particulate composites of piezoelectric

and magnetic oxide grains, 2-2–type laminate ceramic composites consisting of piezoelectric and magnetic oxide layers, and 1-3–type fiber composites with fibers of one phase embedded in the matrix of another phase, as shown in Fig. 1-7. BaTiO$_3$, PZT, PbMgNbO$_3$-PbTiO$_3$, etc., are usually chosen as the piezoelectric ceramic phase, and ferrites usually as the magnetic phase. [7]
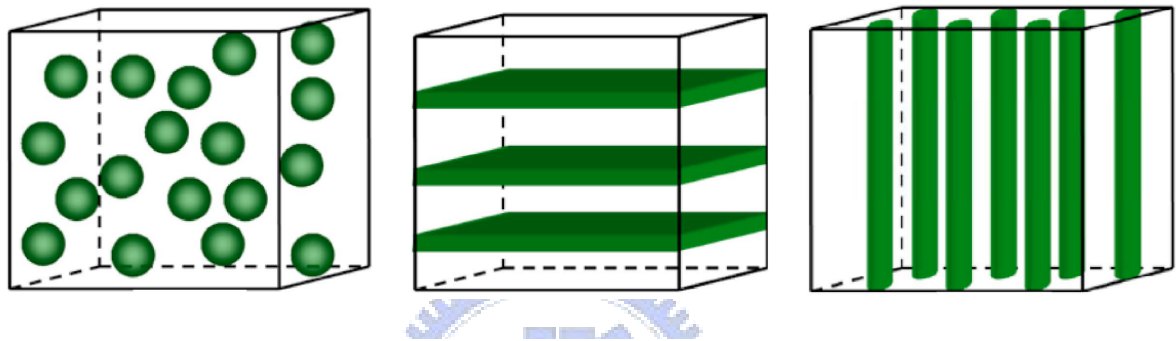
Figure 1-7. Schematic illustration of three bulk composites with the three common connectivity schemes: (a) 0–3 particulate composite, (b) 2–2 laminate composite, and (c) 1–3 fiber/rod composite.

1.3.3   Applications of multiferroics

Multiferroics are of interest for memory and logic device applications, as the coupling between ferroelectric and magnetic properties enables the dynamic interaction between these order parameters. Recently, Ying-Hao Chu performed an experiment of using electric-field to control local ferromagnetism by making the magnetoelectric multiferroic structure. Their work reveals the possibility to locally manipulate ferromagnetism with an electric field for ultra-thin device-scale uses [22].

Besides, promising applications include magnetic field sensors, transducers, filters, oscillators, phase shifters, memory devices, and so on. At the resonance frequency the ME composite can be used as a transducer which converts the microwave magnetic field into a microwave electric field. Because of the shift in the resonance frequency in a static

magnetic or electric bias field the composite materials hold promise in electrically tunable microwave applications such as filters, oscillators, and phase shifters. Due to the hysteretic nature of the ME effect, the composites may find applications in memory devices. This coupling could, in principle, permit data to be written electrically and read magnetically in memory technologies. [7]

1.4 Motivation

1.4.1 Why multiphase magnetoelectric materials

In a single-phase compound, the magnetoelectric effect requires long range atomic moments and electric dipoles. For this reason, the effect is often very weak. On the other hand, the ME coupling of multi-phase multiferroic mediated by mechanical stress at the interface between two phases in a composite has greatly enhanced the magnetoelectric coupling in thin films based on either nanocomposites or superlattices. In this case, by matching a suitable piezomagnetic and an electrostrictive, it can be a suitable way to obtain a large value of the magnetoelectric coefficient and hold great potential for future applications.

1.4.2 Why micro-Raman system

To obtain a fundamental understanding of multiferroics, the experimental observation of the coupling mechanism between the ferroelectric and ferromagnetic orders is of great importance. For multiphase multiferroics, the physical properties at the interfaces is an important aspect to achieve functional multiferroics as the ME interaction happens here. With a scale of single atomic boundary, the polarization and magnetization will reconstruct by chemical bonding, exchange interactions, and strain effects. On the other hand, one can

directly obtain the information about the polarization states and the variation of structure from the phonons in Raman spectra. Phonons at the interface are sensitive to strain induced by lattice mismatch and the broken symmetries. However, very little is known about the behavior of phonons in magnetoelectric multiferroics, even though investigations of phonons have in the past played a crucial role in the understanding of classic ferroelectrics.

Recently, some studies on behaviors of phonons in multiferroics, the variation of phonon energy in spectrum is not obvious and relations between phonon shifting and coupling mechanism are not investigated [23-25]. In our work, we proposed a micro-Raman detection method in which the micro-focused light is employed to measure the coupled interactions across micro hetero-interfaces. Not only the stress dependence of phonon shifting at the interface was observed in Raman spectrum but also the distinct magnetic properties in M-H hysteresis is studying and discussed in three different geometrical $CoFe_2O_4$-$PbTiO_3$ multiferroic systems.

1.5 Organization of the thesis

There are five chapters in this thesis. In Chapter 2, we will introduce the theory of phonon modes in Raman spectra, hysteresis loop of ferromagnetic materials, and X-ray diffraction. Chapter 3 describes the experimental details of sol-gel methods and spin-coating process. We will present the results and discussion about multiphase multiferroics of three geometric structure on the subjects including structure analysis, coupling mechanism induced

phonon modes shifting, and unsaturated magnetization and coercivity.   In the last chapter, we

conclude the investigations on multiphase multiferroics thin film and proposed several topics

worthy of further studying.

References

[1] S. Bhaskar, S. B. Majmder, P. S. Dobal, R. S Katiyar, and S.B. Krupanidhi, J. Appl. Phys. **89**, 5637 (2001).

[2] J. Cheng and Z. Meng, Thin solid films **385**, 5 (2001).

[3] C. H. Wang and D. J. Choi, J. Am. Ceram. Soc. **84**, 207 (2001).

[4] H. Kumazawa and K. Masuda, Thin Solid Films **353**, 144 (1999).

[5] C. Kittel, Introduction to solid state physics, 8th ed., (Wiley, New York, 2004).

[6] R. C. O'Handley, Modern Magnetic Materials, (Wiley, New York, 2000).

[7] C. W. Nan, M. I. Bichurin, S. Dong, D. Viehland and G. Srinivasan, J. Appl. Phys. **103**, 031101 (2008).

[8] E.P. Wohlfarth, Ferromagnetic Materials, Volume 2 (North Holland, 1980).

[9] Young and D. Hugh, University Physics, 8th Ed., (Addison-Wesley, 1992).

[10] V. M. Petrov, G. Srinivasan, M. I. Bichurin and A. Gupta, Phys. Rev. B **75**, 224407 (2007).

[11] Zheng H, Wang J, Lofland SE, Ma Z, Mohaddes-Ardabili L, Zhao T, Salamanca-Riba L, Shinde SR, Ogale SB, Bai F, Viehland D, Jia Y, Schlom DG, Wuttig M, Roytburd A and Ramesh R, Science **303**, 661 (2004).

[12] Ascher E, Rieder H, Schmid H and St"ossel H, J. Appl. Phys. **37,** 1404 (1966).

[13] Smolensky G A, Agranovskaya A I and Isupov V A Sov., Phys. Solid State **1,** 149

(1959).

[14] Smolensky G A, Isupov V A, Krainik N N and Agranovskaya A Isv., Akad. Nauk SSSR, Ser Fiz. **25,** 1333 (1961).

[15] Brixel W, Rivera J P, Steiner A and Schmid H, Ferroelectrics **79,** 201 (1988).

[16] Astrov D. N., Alshin B. I., Tomashpolski Y. Y. and Venevtsev Y. N., Sov. Phys. **28,** 1123 (1969).

[17] Drobyshev L A, Alshin B I, Tomashpolski Y Y and Venevtsev Y N, Sov. Phys., **14,** 634 (1970).

[18] W. Prellier, M. P. Singh and P. Murugavel, J. Phys. Condens. Matter **17,** 7753 (2005).

[19] Junyi Zhai, Zengping Xing, Shuxiang Dong, Jiefang Li, and Dwight Viehland, J. Am. Ceram. Soc., **91,** 351 (2008).
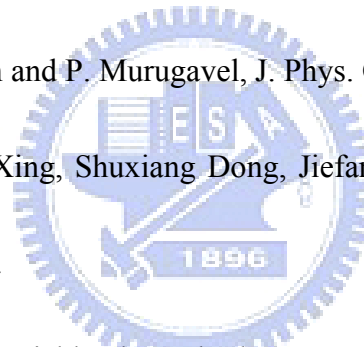
[20] S. Dong, J. F. Li, and D. Viehland, Appl. Phys. Lett. **83**, 2265 (2003).

[21] R. Ramesh and Nicolaa., Nature Materials, **6,** 21 (2007).

[22] Y. H. Chu, Lane W. Martin, Mikel B. Holcomb, Martin Gajek, Shu-Jen Han, Qing He, Nina Balke, Chan-Ho Yang, Donkoun Lee, Wei Hu, Qian Zhan, Pei-Ling Yang, Arantxa Fraile-Rodríguez, Andreas Scholl, Shan X. Wang, and R. Ramesh, Nature Materials, **7,** 478 (2008).

[23] J. Barbosa, B. G. Almeida, J. A. Mendes , A. G. Rolo, J. P. Araújo, and J. B. Sousa, J.Appl. Phys. **101**, 9 (2007).

[24] N. Ortega, A. Kumar, P. Bhattacharya, and Katiyar, R. S., Phys. Rev. B **77**, 10 (2008).

[25] H. M. Zheng, J. Kreisel, Y. H. Chu, R. Ramesh, and Lourdes Salamanca-Riba, Appl. Phys. Lett. **90**, 3 (2007).

Chapter 2 Theoretical Background

2.1 Magnetoelectric Effect [1]

The magnetoelectric response is the appearance of an electric polarization upon applying a magnetic field and the appearance of magnetization upon applying an electric field. The coupling interaction between ferroelectric and ferromagnetic materials in multiphase multiferroics has been found to be due to elastic interaction as was the case in bulk composites.

Magnetic-field-induced electric polarization (MIEP) in nanostructured multiphase multiferroic composite films was studied by using the Green's function approach. As the coupled interaction between ferroelectric and ferromagnetic phases in the multiferroic nanostructures is an elastic interaction, the constitutive equations for the coupling magnetic-mechanical-electric interactions in the nanostructured films can be expressed by direct notation for tensors as

$$\sigma = c\varepsilon - e^{T}E - c\varepsilon^{ms} - \sigma_{s},$$
$$D = e\varepsilon + \kappa E + \alpha H + P_{s}, \qquad (2.1\text{-}1)$$
$$B = \mu(\varepsilon, E, H)H + M_{s},$$

where σ, ε, **D**, **E**, **B**, and **H** are the stress, strain, electric displacement, electric field, magnetic induction, and magnetic field, respectively; **c** and **κ** are, respectively, the stiffness at constant fields and the dielectric constant at constant strain; the permeability μ strongly depends on ε and electric and magnetic fields; **e** (**e**^{T} being the transpose of **e**) is the piezoelectric coefficient;

21

and ε^{ms} is the magnetostrictively induced strain related with the magnetic field dependent magnetostriction constants (e.g., λ_{001} and λ_{111}) of the ferromagnetic phase; α is the magnetoelectric coefficient.   These are the same as the case for bulk multiferroic composites. However, in comparison to the bulk composites, there exist remarkable residual stress σ_s (or residual strain ε_s), spontaneous polarization $\mathbf{P}_s$ and magnetization $\mathbf{M}_s$ in the multiferroic films.

The effective properties (denoted by the starred quantities below) of the multiferroic films can still be defined as the averaged fields (denoted by $<\ >$), e.g., $<\mathbf{D}> = \mathbf{e}^*<\varepsilon> + \kappa^*<\mathbf{E}> + \alpha^*<\mathbf{H}> + \mathbf{P}$s.   We considered the ME effect of such nanostructured films.   Under only applied magnetic field, the effective polarization in the mechanically clamped films is

$$\bar{P} = \alpha^* < H > + \bar{P}_s \tag{2.1-2}$$

In a state of static equilibrium,

$$\frac{\partial \sigma_{ij}(x)}{\partial x_j} = \frac{\partial D_i(x)}{\partial x_i} = \frac{\partial B_i(x)}{\partial x_i} = 0 \tag{2.1-3}$$

By solving the equilibrium equations (2.1-3) under the homogeneous magnetic-mechanical-electric ($\mathbf{H}^0$-ε^0-$\mathbf{E}^0$) boundary conditions in terms of the Green's function approach [2], the local fields within the composite films can be obtained as

$$\begin{aligned}
\varepsilon &= \varepsilon^0 + G^u(c-c^o) + G^u e^T E - G^u(c\varepsilon^{ms} + \sigma_s), \\
E &= E^0 + G^\phi e\varepsilon + G^\phi(\kappa - \kappa^0)E + G^\phi(\alpha H + P_s), \\
H &= H^0 + G^\psi(\mu - \mu^0)H + G^\psi M_s,
\end{aligned} \tag{2.1-4}$$

where, c^0, κ^0, and μ^0 represent the constitutive constants of a homogeneous reference medium;

22

$\mathbf{G}^u$, $\mathbf{G}^\Phi$, and $\mathbf{G}^\Psi$ are the modified displacement, electric and magnetic potential Green's functions for the homogeneous medium [2, 3]. Substitution of Eq. (2.1-4) into (2.1-1) directly gives explicit solutions for the local σ, $\mathbf{D}$, and $\mathbf{B}$, also as a function of ε^0, $\mathbf{E}^0$, and $\mathbf{H}^0$. By averaging these solutions for local field quantities and eliminating ε^0, $\mathbf{E}^0$, and $\mathbf{H}^0$ from them, one can get the effective polarization in the mechanically clamped films as

$$\vec{P} = < P_s + (\kappa - \kappa*)T^{33}G^\phi[P_s - eT^{66}G^u(c\varepsilon^{ms} + \sigma_s)] \\ + (e*-e)T^{66}G^u(c\varepsilon^{ms} + \sigma_s + e^T T^{33}G^\phi P_s) >,$$

(2.1-5)

where $\mathbf{T}^{66}$ and $\mathbf{T}^{33}$ are two so-called t-matrix tensors. This equation is quite general and independent of the models assumed for the topology of the phases in the composite film.

For the (00l)-oriented multiferroic nanostructure, only the volume average is necessary in Eq. (2.1-5). Ferroelectric phase is taken as the homogeneous reference medium, since the ferroelectric phase with high volume fraction is a matrix phase. Furthermore due to the fact that $\mathbf{e} = \mathbf{0}$ and $\mathbf{P_s} = 0$ for the ferromagnetic phase, $\varepsilon^{ms} = 0$ and $\mathbf{Ms} = 0$ for the ferroelectric phase, and $\alpha = 0$ for both phases, Eq. (2.1-5) can be rewritten as

$$\vec{P} = (1-f)\{P_s + (\kappa^p - \kappa*)G^\phi(P_s - e^p G^u \sigma_s^p) \\ + (e*-e^p)G^u(\sigma_s^p + e^T G^\phi P_s)\} \\ + fe*[I - G^u(c^m - c^p)]^{-1}(c^m \varepsilon^{ms} + \sigma_s^m),$$

(2.1-6)

$H_3 \uparrow \quad P_3 \uparrow$

(a)

(b)
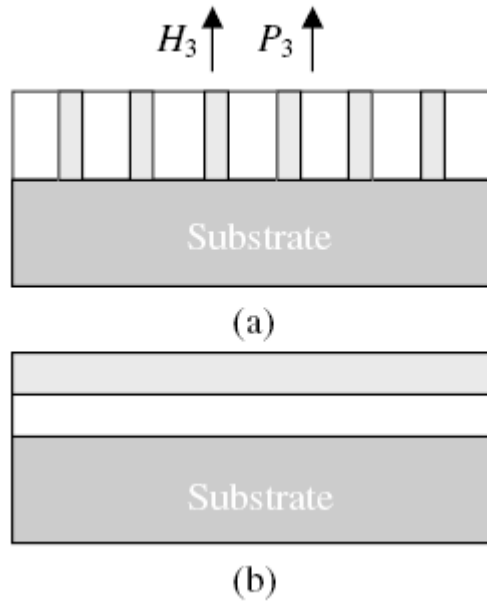
Fig. 2-1 Schematic illustration of the nanostructured multiferroic BaTiO$_3$-CoFe$_2$O$_4$ films in (a) the 1-3 type where the CoFe$_2$O$_4$ nanopillars (shaded) are embedded in the BaTiO$_3$ matrix, and in (b) the 2-2 type where the BaTiO$_3$ layer is first deposited on the substrate SrRuO$_3$ and then the CoFe$_2$O$_4$ layer (shaded) on the piezoelectric layer.
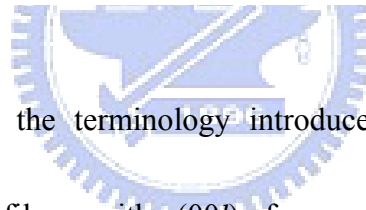
For the 1-3 type (using the terminology introduced by L. E. Cross and co-workers) nanostructured composite films with (00l) ferromagnetic nanopillars embedded in a ferroelectric matrix, the effective electric polarization **P** along the symmetric direction is easily obtained from Eq. (2.1-6) as

$$\bar{P}_3 = (1-f)\,P_{s3} + \frac{2f(1-f)e_{31}^p}{\bar{k} + c_{11}^p - c_{12}^p}(\sigma_{11}^p - \sigma_{11}^m). \tag{2.1-7}$$

In this case that the height of pillars is much larger than their diameter (e.g., 20–30 nm in diameter and 400 nm in height for nanopillars), where $\bar{k} = f(c_{11}^p + c_{12}^p) + (1-f)(c_{11}^m + c_{12}^m)$; σ_{11}^p and σ_{11}^m are in-plane total stresses including residual stresses and magnetostrictively

induced stresses, respectively, in the ferroelectric and ferromagnetic phases, and are expressed as

$$\sigma_{11}^{p(m)} = \left(c_{11}^{p(m)} + c_{12}^{p(m)}\right)\varepsilon_{11}^{p(m)} + c_{13}^{p(m)}\varepsilon_{33}^{p(m)},$$

(2.1-8)

where $\varepsilon_{11}^{p(m)}$ and $\varepsilon_{33}^{p(m)}$ are in-plane and out-of-plane total strains including residual strains (ε_{s11} and ε_{s33}) and magnetostrictively induced strains (ε_{ij}^{ms}) upon applying the magnetic field, respectively, in the ferroelectric and ferromagnetic phases, e.g., $\varepsilon_{11}^{m} = \varepsilon_{11}^{ms} + \varepsilon_{s11}^{m}$ and $\varepsilon_{33}^{m} = \varepsilon_{33}^{ms} + \varepsilon_{s33}^{m}$. At zero magnetic field, ε_{ij}^{p} and ε_{ij}^{m} are equal to their residual strains, i.e., $\varepsilon_{ij}^{p}(H=0) = \varepsilon_{sij}^{p}$ and $\varepsilon_{ij}^{m}(H=0) = \varepsilon_{sij}^{m}$.

For the 2-2 type nanostructured composite films with (00l) ferroelectric and ferromagnetic nanolaminates as shown in Fig. 1(b), the effective electric polarization $\bar{P}_3$ can also be directly obtained from Eq. (2.1-6) as

$$\bar{P}_3 = (1-f)\frac{\kappa_{33}^{m}}{\bar{\kappa}_{33}}P_{s3} + \frac{f(1-f)e_{33}^{p}\kappa_{33}^{m}}{\bar{c}_{33}\bar{\kappa}_{33}}(\sigma_{33}^{p} - \sigma_{33}^{m}),$$

(2.1-9)

in the case that the thickness of a layer (e.g., 30 nm [4]) is much less than the macroscopic size of the film plane, where $\bar{c}_{33} = fc_{33}^{p} + (1-f)c_{33}^{m}$, $\bar{\kappa}_{33} = f\kappa_{33}^{p} + (1-f)\kappa_{33}^{m}$; σ_{33}^{p} and σ_{33}^{m} are out-of-plane total stresses including residual stresses and magnetostrictively induced stresses, respectively, in the ferroelectric and ferromagnetic phases, and are expressed as

$$\sigma_{33}^{p(m)} = 2c_{13}^{p(m)}\varepsilon_{11}^{p(m)} + c_{33}^{p(m)}\varepsilon_{33}^{p(m)}.$$

(2.1-10)

At zero magnetic field, $\varepsilon_{11}^{p(m)}(H=0) = \varepsilon_{s11}^{p(m)}$ and $\varepsilon_{33}^{p(m)}(H=0) = \varepsilon_{s33}^{p(m)} = 0$.

25

These explicit equations show that the effective electric polarization is sensitive to residual strains and spontaneous polarization in the films, materials constants of the two phases and the ways of their combination, and applied magnetic field. Of particularly interesting to note is that a large ME effect is obtained in the 1-3 films at room temperature. When the applied magnetic field increases from zero up to 240 kA/m ($\approx$ 0.3 T), the ME effect of the 1-3 multiferroic $BaTiO_3$-$CoFe_2O_4$ film is about 400 $\mu C/m^2$, comparable with that in monophase RMnO3 observed at low temperature and high magnetic field [5]. In comparison, the MIEP in the 2-2 $BaTiO_3$-$CoFe_2O_4$ film is quite low and much less than that in the 1-3 type. The main reason is attributed to the tremendous clamping effect in the 2-2 type film, where the in-plane gigantic constraint effect greatly inhibits the magnetostriction. For comparison, the 1-3 and 2-2 bulk composites [2] of $BaTiO_3$-$CoFe_2O_4$ were calculated as well, as shown in Figure 2-2, where the residual stress σ_s and the spontaneous polarization **Ps** were neglected. As seen, the 1-3 bulk composites exhibit lower MIEP than the 1-3 nanostructured counterparts, and the 2-2 bulk composites also exhibit lower MIEP than the 1-3 type.
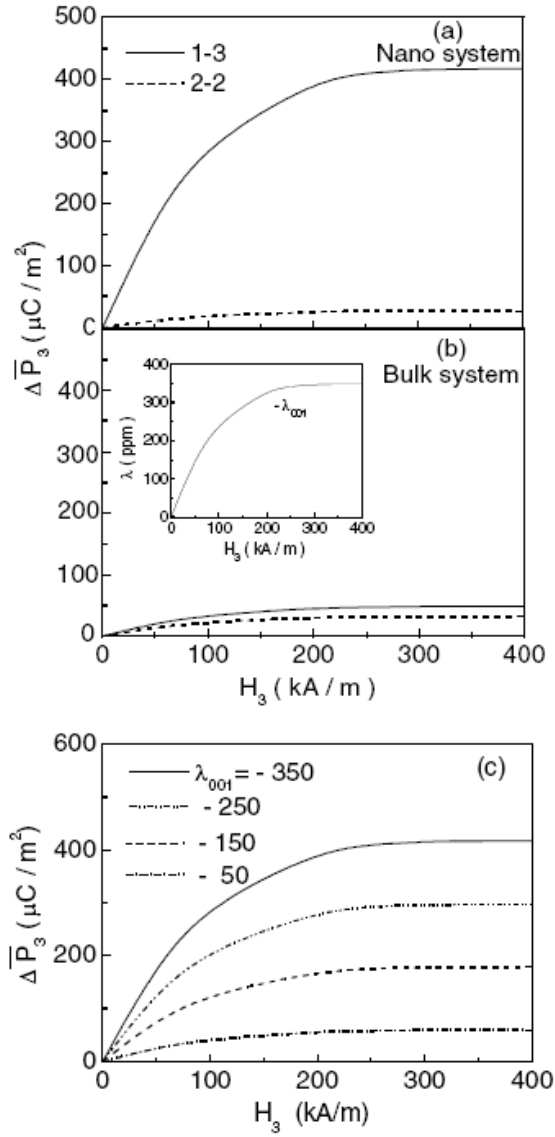
Fig. 2-2 Dependence of the magnetic-field-induced polarization P_3 on the magnetic field for (a) the nanostructured films and (b) the bulk composites of $BaTiO_3=CoFe_2O_4$ with $f = 0.35$ at room temperature. The inset in (b) is the magnetostrictive behavior taken for $CoFe_2O_4$. (c) Effect of the magnetostriction of the ferromagnetic phase on P_3 for this 1-3 type films.   [After Nan ref.1]
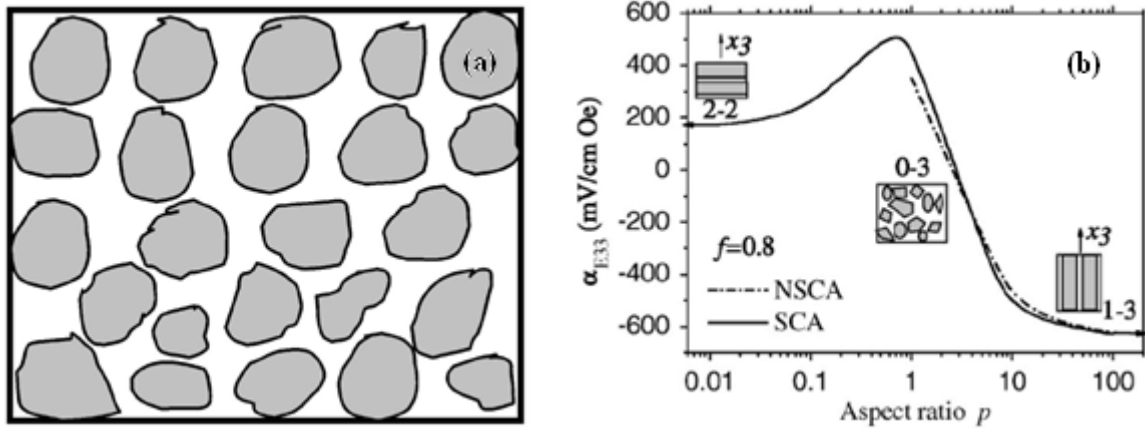
Fig. 2-3 Diagram of 0-3 composite and the ME response: (a) 0-3 multiferroic composite with high concentration of particulate magnetic phase well dispersed in the piezoelectric phase. (b) ME response of $CoFe_2O_4$-$BaTiO_3$ ceramics plots as a function of effect of the grain shapes and phase connectivity. [After Nan ref. 10]

The 0-3 particular composites with ferrite grains in ferroelectric matrix were also calculated by the same method. It is obvious that the grain shape and phase connectivity have a significant effect on the ME response of the composites. Right hand side of the Fig. 2-3 shows the 1-3 type obtains high ME response while the 0-3 type is quite low.

2.2 Raman Scattering Theorem

Infrared (IR) and Raman spectroscopy both measure the vibration energies of molecules but these methods rely on different selection rules. The possible vibrations of a molecule are sensitive to IR absorption if the vibration results in a change in the dipole moment. However, for a vibration to be Raman active, the polarizability of the molecule must change with the vibrational motion. For bonds with a strong dipole moment (which are IR active) the polarizability is usually low. For bonds which have a weak dipole moment (which are IR

inactive) the polarizability is usually high and the vibrational states of the bond are Raman active. IR and Raman activity are complimentary and the two techniques are used to fully characterize the vibrational states of molecules.

For infra-red (IR) wavelengths, absorption must in some way be related to a variation in the dipole moment associated with molecule. One atom of the molecules has a local charge Δq then the rest of atoms have charge - Δq and the dipole moment μ, is given by

$$\mu = \Delta q \cdot l,$$

(2.2-1)

where l is the separation of the charges.

Electromagnetic wave can be absorbed or emitted by a medium if during its interaction there is a change in the charge distribution within the medium. During the interaction with photon, the dipole moment μ will change, thus can rewrite the dipole moment as

$$\mu = \mu_0 + \frac{\partial \mu}{\partial Q} Q,$$

(2.2-2)

where $Q = (r - r_{eqm})$ is the displacement from the equilibrium positions r_{eqm}. The total Hamiltonian is described as

$$H = H_0 + H_{int},$$

(2.2-3)

where $H_{int} = E \cdot \mu$ expresses the interaction of an atom with a photon to the unperturbed Hamiltonian H_0.

Thus the transition moment, R can be written as

$$R = \int \psi_i H_{int} \psi_f = \langle i | H_{int} | f \rangle \qquad (2.2\text{-}4)$$

thus,

$$R = \langle i | (\mu_0 + Q \frac{\partial \mu}{\partial Q}) \cdot E | f \rangle = \langle i | \frac{\partial \mu}{\partial Q} \cdot E | f \rangle . \qquad (2.2\text{-}5)$$

IR absorption occurs as the transition $R \neq 0$, in other words there must be a change in the dipole moment due to vibration of the molecule which is induced by the applied field E, since the transition probability P is equal to R^2. The condition that an IR absorption or emission must be associated with a change in dipole moment is known as the dipole selection rule. The dipole selection rule plays an important role in IR spectroscopy because it tells us whether a molecule will be IR active or not.

When light passes through a medium, most of the light is reflected, transmitted, absorbed, elastic scattered, or inelastic scattered. Raman scattering is an inelastic scattering process. Consider the light encounters the medium, the electromagnetic field of the incident radiation, E, interacts inelastically with a molecule. The electric field may induce an electric dipole in the molecule, given by

$$P = \alpha \bullet E, \qquad (2.2\text{-}6)$$

where α is referred to as the polarizability of the molecule and P is the polarization, defined as dipole moment per unit volume. The variation of α is correlated to the crystal coordinate

system in which the molecule vibrates and it can be expressed as:

$$\alpha = (\alpha)_0 + (\frac{\partial \alpha}{\partial \theta})_0 \theta. \qquad (2.2\text{-}7)$$

If the vibration is simple harmonic oscillating:

$$\theta = \theta_0 \cos 2\pi v_m t , \qquad (2.2\text{-}8)$$

where θ_0 is amplitude and v_m is the vibrational frequency. Assume a monochromatic

incident EM wave of frequency v_0 has electric field:

$$E = E_0 \cos 2\pi v_0 t \qquad (2.2\text{-}9)$$

Combing the equations above

$$
\begin{aligned}
P &= [(\alpha)_0 + (\frac{\partial \alpha}{\partial \theta})_0 \theta_0 \cos 2\pi v_m t] E_0 \cos 2\pi v_0 t \\
&= (\alpha)_0 E_0 \cos 2\pi v_0 t + \frac{1}{2} E_0 \theta_0 (\frac{\partial \alpha}{\partial \theta})_0 \cos 2\pi (v_0 - v_m) t \qquad (2.2\text{-}10) \\
&+ \frac{1}{2} E_0 \theta_0 (\frac{\partial \alpha}{\partial \theta})_0 \cos 2\pi (v_0 + v_m) t.
\end{aligned}
$$

From Eq. (2.2-10), the three different scattering processes of linearly electric dipole moments

are respectively, Rayleigh scattering possessing the same frequency with incoming light v_0,

the Stoke scattering with a low frequency of $v_0 - v_m$, and the high frequency $v_0 + v_m$ known

as anti-Stoke lines.   Those lines on the low frequency side of the exciting lines (i.e., $\upsilon_0 - \Delta\upsilon_i$, i

= 1, 2…….) are always matched by lines on the high frequency side (i.e., $\upsilon_0 + \Delta\upsilon_i$, i = 1,

2…….) but the latter are much weaker when the scattering medium is at room temperature.

Raman scattering is inherently a weak process, but laser provides enough intensity that the

spectra can be routinely measured.

The incident phonon loses its energy by producing a phonon (Stokes shifted), or gain energy and momentum by absorbing a phonon (anti-Stokes shifted), according to the energy and momentum conservation rules:

$$h\nu_s = h\nu_i \pm h\Omega \text{ ,}$$

(2.2-6)

$$q_s = q_i \pm K \text{ ,}$$

(2.2-7)

where υ_0 and υ_s are the incoming and scattered phonon frequencies, q_i and q_s are the incoming and scattered phonon wavevectors, Ω and K are the phonon frequency and wavevector, respectively.

All the Raman mode frequencies, intensities, line-shape, and line-width, as well as polarization can be used to characterize the lattice and impurities. The intensity gives information on crystallinity. The line-width increases when a material is damaged or disordered, because damage or disorder occurs in a material will increase phonon damping rate or relax the rules for momentum conservation in Raman process. All these capabilities can be used as a judgment for layered microstructure as well as bulk materials, subject only to the limitation that the penetration depth of the exciting radiation range from a few hundred nanometers to few micrometers.

2.2.1 Phonon Modes of PbTiO$_3$ System

PbTiO$_3$ belongs to the O_h^1 (*P3m3*) space group, with one formula unit per primitive cell, in the cubic (paraelectric) phase (see Table 2-1 [6]).   Thus there are 12 optic modes at the Γ point of the Brillouin zone.   The optic modes transform the $3T_{1u} + 2T_{2u}$ irreducible representations of the O_h point group.   The T_{1u} modes are infrared active and T_{2u} is the so-called "silent mode" since it is neither infrared nor Raman active.

In the ferroelectric tetragonal phase [C_{4v}^1 (*P4mm*) space group] each triply degenerate T_{1u} mode splits into two modes transforming as the $A_1 + E$ irreducible representations of the C_{4v} point group.   The silent mode also, in principle, splits into $B_1 + E$ modes that are Raman active; so that the single feature that one measures for these phonons is $B_1 + E$ modes. However, because of the long-range electrostatic forces, the situation for the T_{1u} modes is more complicated.   Each of these optic modes can have a polarization transverse to the direction of propagation (TO modes) as well as polarization along the direction of propagation (LO modes).

Table 2-1 Phonon frequencies (cm^{-1}) in $PbTiO_3$ single crystal and thin film [After I. Tauchi [9]]

| Phonon mode | Single crystal | | Thin film |
	$P \sim 0$ GPa	$P \sim 1.35$ GPa	Pt/Si
E(1TO)	89	80	80
A1(1TO)	127	117	118
E(2TO)	221	201	209
B1+E	290	287	289
A1(2TO)	364	336	334
E(2LO)+A1(2LO)	445	-	443
E(3TO)	508	504	504
A1(3TO)	651	607	604
E(3LO)+A1(3LO)	717	746	728

2.2.2 Phonon Modes of $CoFe_2O_4$ System

Spinel $CoFe_2O_4$, a cubic ferromagnetic oxide with high coercivity, moderate saturation magnetization, as well as remarkable chemical stability and mechanical hardness, has been extensively studied. Spinels can be divided into two kinds according to their structures. One is 'normal' spinel, with all the divalent (A) cations on the tetrahedral (T) sites and the trivalent (B) cations on the octahedral (O) sites, which can be represented by the formula $A(BB)O_4$. The other is 'inverse' spinel, $B(AB)O_4$, in which the divalent cations occupy the O-sites and the trivalent cations are equally divided among the T- and remaining O-sites.

$CoFe_2O_4$ has a cubic inverse-spinel structure with $O_h^7 (F\bar{d}3m)$ space group, which gives rise to 39 normal modes:

$$\Gamma = A_{1g} + E_g + F_{1g} + 3F_{2g} + A_{2u} + 2E_u + 4F_{1u} + 2F_{2u},$$

where five optic modes are Raman active ($A_{1g} + 1E_g + 3F_{2g}$) and four are infrared active ($4F_{1u}$).

Shebanova et al., [7] performed polarized experiments on an oriented single crystal providing a new interpretation of the Raman spectrum with the following assignment for symmetries of the observed modes: A_{1g} for 668 cm^{-1}, E_g for 306 cm^{-1}, and T_{2g} for 538, 193, and 450 - 490 cm^{-1}. Since Fe_3O_4 with the cubic inverse-spinel structure belonging to the same space group as $CoFe_2O_4$ has been widely investigated, we can take the Raman spectra of Fe_3O_4 as a reference. Table 2-2 shown below shows the experimental assignment on the Raman active modes of Fe_3O_4 from different authors.

The primitive unit cell of magnetite (Figure 2-4) [7] contains one unit where iron atoms are coordinated octahedrally (D_{3d}), and two FeO_4 units with the tetrahedral coordination (Td). Group-theoretical and lattice-vibration analyses based on the quasimolecular description of the spinel structure have led to the following description of normal mode motions of the FeO_4 tetrahedron: A_{1g} - symmetric stretch of oxygen atoms along Fe-O bonds, E_g and T_{2g} (3) - symmetric and asymmetric bends of oxygen with respect to Fe, respectively, T_{2g} (2) - asymmetric stretch of Fe and O, T_{2g} (1) - translatory movement of the whole FeO_4. There are zero, or close-to-zero displacements of Fe atoms in modes A_{1g}; E_g; and T_{2g} (3).
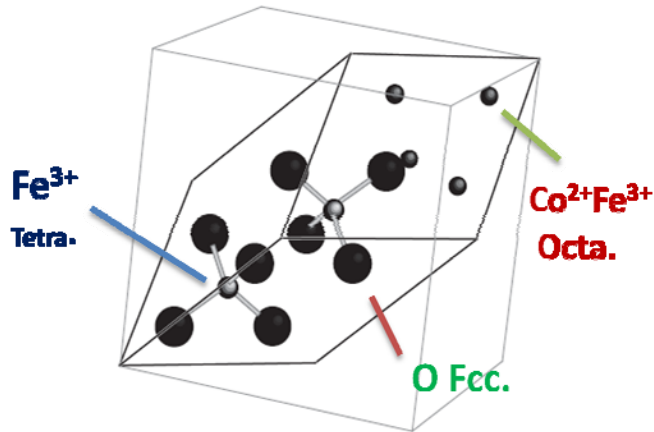
35

Figure 2-4 Primitive unit cell of magnetite.

Table 2-2 Summary of the symmetry assignments of Raman modes on magnetite [7]

Raman shift	Mode symmetry					
	Shebanova	**Gasparov**	**Degiorgi**	**Graves**	**Verble**	**Hart**
668	A_{1g}	A_{1g}	A_{1g}	A_{1g}	A_{1g}	A_{1g}
538	$T_{2g}(2)$	T_{2g}	E_g or T_{2g}	A_{1g}	$T_{2g}(2)$	T_{2g}
450-490	$T_{2g}(3)$		Magnon	T_{2g}		Magnon
306	E_g	T_{2g}	T_{2g}	E_g	$T_{2g}(3)$	E_g
193	$T_{2g}(1)$	T_{2g}		T_{2g}		

2.3 X-ray Diffraction

X-ray scattering techniques are a family of non-destructive analytical techniques which reveal information about the crystallographic structure, chemical composition, and physical properties of materials and thin films. These techniques are based on observing the scattered intensity of an x-ray beam hitting a sample as a function of incident and scattered angles, polarization, and wavelength or energy.

X-ray diffraction techniques are based on the elastic scattering of x-rays from structures that

have long range order.   A crystal consists of a regular array of atoms, each of which can

scatter electromagnetic waves.   A monochromatic beam of X-ray that falls on a crystal will be

scattered in all directions, in certain directions the scattered waves will constructively interfere

with one another while others will destructively interfere.   The analysis was developed in

1913 by W. L. Bragg.   The condition which must be fulfilled for radiation scattered by crystal

atoms to undergo constructive interference can be obtained from a diagram like that in Figure

2-5.   In the plane wave description, a beam containing x-rays of wavelength λ impinges on a

crystal at an angle θ with a family of Bragg planes, whose space is *d*.   The beam goes past

atom A in the first plane and atom B in the next, and each of them scatters part of the beam in

random directions.   Constructive interference occurs only between those scattered rays whose

paths differ by exactly λ, 2λ, 3λ, and so on.   That is, the path difference must be nλ, where n is

an integer.   The only rays scattered by A and B for which this is true are those labeled I and J
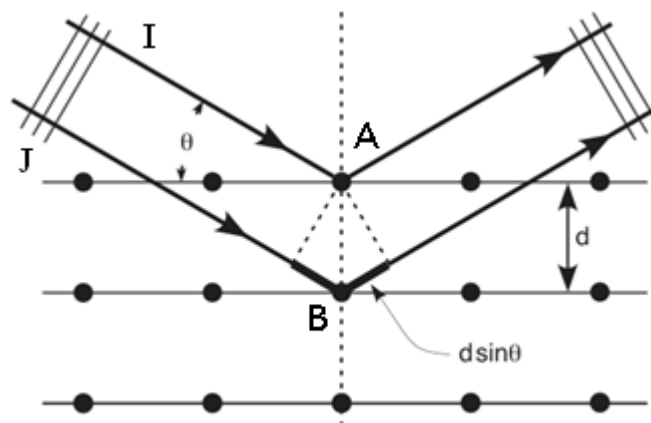
in Figure 2-4.

Figure 2-5 Diffraction of x-ray.   Incoming beam causes each scatter to re-radiate a small portion of its energy as a spherical wave.   If scatters are arranged symmetrically with a separation d, these spherical waves will add constructively only in directions where their path-length difference $2d \sin \theta$ equals an integer multiple of the wavelength λ.   In that case, part of the incoming beam is deflected by an angle 2θ, producing a *reflection* spot in the diffraction pattern.

The first condition on I and J is that their common scattering angle is equal to the angle of incidence θ of the original beam.   The second condition is that

$$2d \sin \theta = n\lambda, n = 1, 2, 3 \ldots, \tag{2.3-1}$$

where d is the spacing between diffracting planes, θ is the incident angle, n is any integer, and λ is the wavelength of the beam.   Since the ray J must travel the distance $2d\sin\theta$ farther than ray I. The integer n is the order of the scattered beam.   Then considering a tetragonal unit cell as shown in Figure 2-6 which is characterized by lattice parameters a and c.   The inter-plane spacing d for the hexagonal structure is given as:

$$\frac{1}{d_{hkl}^2} = \frac{h^2 + k^2}{a^2} + \frac{l^2}{c^2} \tag{2.3-2}$$
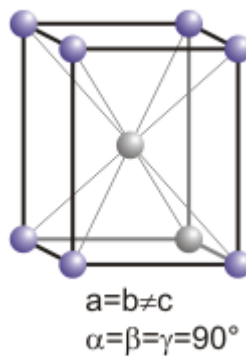

$$a=b \neq c$$
$$\alpha = \beta = \gamma = 90°$$

Fig. 2-6 Structure of tetragonal crystal: lattice constants in its unit cell is a=b≠c.

Combing Bragg's law with Eq. 2.3-1

$$\frac{1}{d_{hkl}^2} = \frac{h^2 + k^2}{a^2} + \frac{l^2}{c^2} = \frac{4\sin^2\theta}{\lambda^2}$$

(2.3-3)

and rearranging Eq. 2.3-3 gives

$$\sin^2\theta = \frac{\lambda^2}{4}\{\frac{h^2 + k^2}{a^2} + \frac{l^2}{c^2}\}.$$

(2.3-4)

The lattice parameters a and c can be determined by simultaneously fitting the diffraction

angles of different reflections using Eq. 2.3-4.

For a cubic crystal with lattice constant a, the equation can be written as

$$\sin^2\theta = \frac{\lambda^2}{4}\{\frac{h^2 + k^2 + l^2}{a^2}\}.$$

(2.3-5)

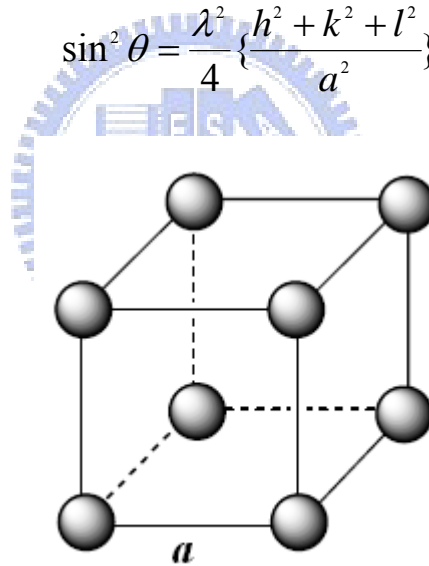

Fig. 2-7 Simple cubic structure with lattice constants a = b = c.

References

[1] C.W. Nan, G. Liu, and Y. Lin, Phys. Rev. Lett. **94** 197203 (2005).

[2] C.W. Nan, M. Li, X. Q. Feng, and S. Yu, Appl. Phys. Lett. **78**, 2527 (2001); C.W. Nan, M. Li, and J. H. Huang, Phys. Rev. B **63**, 144415 (2001).

[3] C.W. Nan, Phys. Rev. B **50**, 6082 (1994); C.W. Nan, Y. H. Lin, and J. H. Huang, Ferroelectrics **280**, 153 (2002).

[4] H. Zheng *et al.*, Science **303**, 661 (2004).

[5] T. Kimura et al., Nature **426**, 55 (2003); T. Goto et al., Phys. Rev. Lett. **92**, 257201 (2004). N. Hur et al., Nature **429**, 392 (2004).

[6] D. S. Fu, H. Iwazaki, H. Suzuki and K. Ishikawa, J. Phys. Condens. Matter **12,** 399 (2000).

[7] O. N. Shebanova, and P. Lazor, J. Solid State Chem **174,** 424 (2003).

[8] Dana ES, Ford WE "A Textbook of Mineralogy," fourth edition New York: John Wiley & Sons p **28** (1932).

[9] I. Taguchi, a, A. Pignolet, L. Wang, M. Proctor, F. L&y, and P. E. Schmid, J. Appl. Phys. **73**, 394 (1993).

[10] C.W. Nan, M. I. Bichurin, Shuxiang Dong, D. Viehland, and G. Srinivasan, J. Appl. Phys. **103,** 031101 (2008).

Chapter 3 Experimental Details

3.1 Thin Film Preparation

3.1.1   0-3 type PTO-CFO system

We used simple solution method to fabricate three different geometric forms of the

$PbTiO_3$-$CoFe_2O_4$ multiferroics, which are respectively CFO discs aligned in PTO matrix

(disk-3 type), the CFO and PTO multilayered structure (2-2 type), and the CFO particles

embedded in PTO matrix (0-3 type) as shown in Figure 3-1.
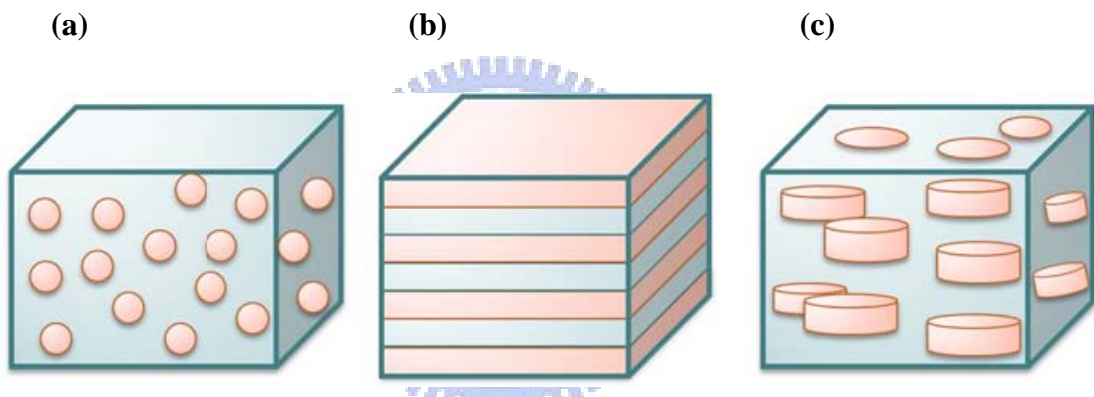
Fig. 3-1 Schematic illustration of three thin films with different connectivity schemes: (a) the 0-3 type with CFO particles embedded in PTO matrix, (b) the 2-2 type with CFO and PTO nanolayers, and (c) the disk-3 type with CFO disc aligned in PTO matrix.

The gel of $PbTiO_3$ was produced by dissolving the lead acetate trihydrate and titanium

isopropoxide into the 2-methoxyethanol to stir and heat for 30 min.   The 0.3M $CoFe_2O_4$ gel

was made from the cobalt nitrate hexahydrate and iron nitrate enneahydrate by the same

process.   Pure PTO gel was then spin-coated on Si and Pt/Si and CFO on Pt/Si substrate as

the reference samples.

The 0-3 type is made of dispersing CFO particles in PTO matrix.   First the CFO

41

particles were obtained by drying solution then grinded, annealed, and grinded again to get granular morphology. The CFO particles about 100 nm were then put into the $PbTiO_3$ solution with molar ratio 0.8:1 and shaken until they were well-mixed in the solution. Finally the resultant solution was spin-coated 5 layers on Pt/Si substrate and the 0-3 film was finished after annealing at 750 ℃ for 1.5 hrs.

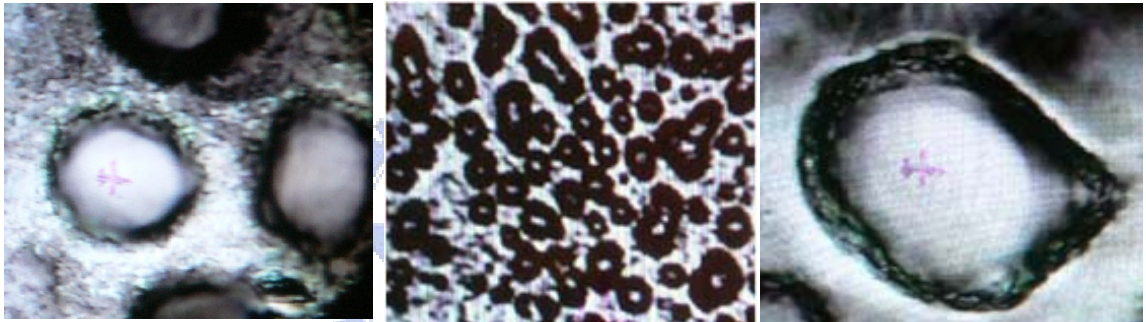### 3.1.2   Disk-3 type PTO-CFO system

Fig. 3-2 Top view images of the OM pictures in disk-3 film.   PTO and CFO possessing pervoskite and spinel structure individually precipitated in this self-assembled type [7]: the CFO formed disks while the PTO was the matrix.   The thickness of the disks was 2 μm and the radius of disk was about 5 μm; hence we named this type as "disk-3" but not "1-3" type.

The disk-3 type CFO-PTO samples were prepared by coating four PTO layers then another four CFO layers alternatively.   Finally, the 4p/4c/4p/4p/4c/4p/Pt/Si film was annealed at 750℃ for 1.5 hours, where "n"p and "n"c stands for successively coated n layers of PTO and CFO, respectively.   The top view images of the disk-3 type by using the optical microscopy (OM) system was found consisting of sub-10 μm CFO disc embedded in PTO matrix rather than nanometer sized CFO rods in PTO matrix [1] due to the higher annealing

temperature. After coating CFO layers and heating it on hot plate, the CFO disc formed.
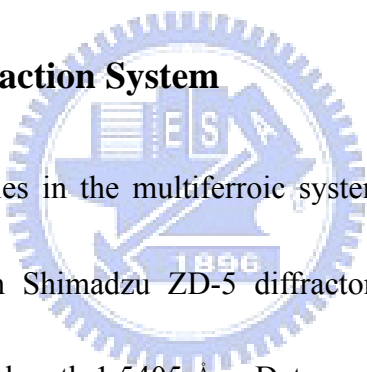The reason is that the cohesion of CFO gel is stronger than the adhesive force between CFO
gel and PTO one. It reveals the similar morphology as illustration in Figure 3-1(c).

3.1.3   2-2 type PTO-CFO system

The process of making the 2-2 type with 2p/2c/2p/2c/2p/2c/2p/Pt/Si stacking layers is the
same as the disk-3 type except that the every layer was individually annealed at 500 ℃ for 3
minutes and finally annealed at 700 ℃ for 1.5 hours.

3.2 Characterization

3.2.1   X-ray Diffraction System

The study of the samples in the multiferroic systems were accomplished using X-ray
power diffraction (XRD) in Shimadzu ZD-5 diffractometer and monochromatic in high
intensity Cu-Kα line of wavelength 1.5405 Å. Data were recorded between the angle range
$20^0 < 2\theta < 60^0$ with steps of 0.04^0. The maximum voltage of the system is 30 KV, with the
maximum current 20 mA and rate of scanning is 4^0/min. The resulting XRD patternts were
Gaussian fitted to get the diffraction peak positions and widths. By comparing with the
JCPD data, the fitted peak positions and corresponding reflection planes were used to
calculate the lattice constants.

3.2.2   Raman Detection System

Raman spectroscopy consists mainly of three components: laser system, spectrometer,

and computer.   An-ion laser (Coherent INNOVA 90) provides an excitation source of a

wavelength 488 nm.   The unwanted plasma lines were filtered out by a laser-line filter.   A

biconvex spherical lens with a focal length of 5 cm was used to focus the laser beam onto the

sample surface at 45 degree reflection geometry.   The laser power on the sample surface is

about 30~35 mW with beam spot size of 30~50 μm (in diameter).   The scattered light was

collected by a camera lens and imaged onto the entrance slit of a spectrograph (Spex

triplemate1877C) which is equipped with a liquid-nitrogen cooled charge coupled device

(CCD) detector array (Phometrics CC200).

3.2.3   Magnetization Measurement System

The magnetic properties viz. saturation magnetization, coercivity and retentivity of samples

have been determined from the magnetic moment versus magnetization curve recorded for

various samples with the help of superconducting quantum interference device (SQUID)

system.

SQUID is very sensitive magnetometer used to measure extremely small magnetic fields,

based on superconducting loops containing Josephson junctions.   They are sensitive enough

to measure fields as low as 5×10^{-18} T within a few days of averaged measurements [2].

There are two main types of SQUID: DC and RF.   The DC SQUID was invented in 1964 by

Arnold Silver, Robert Jaklevic, John Lambe, and James Mercereau of Ford Research Labs

after B. D. Josephson postulated the Josephson effect in 1962 and the first Josephson Junction was made by John Rowell and Philip Anderson at Bell Labs in 1963. The RF SQUID was invented in 1965 by James Edward Zimmerman and Arnold Silver at Ford. The traditional superconducting materials for SQUIDs are pure niobium or a lead alloy with 10% gold or indium, as pure lead is unstable when its temperature is repeatedly changed. To maintain superconductivity, the entire device needs to operate within a few degrees of absolute zero, cooled with liquid helium. "High temperature" SQUID sensors are more recent; they are made of high temperature superconductors, particularly YBCO, and are cooled by liquid nitrogen which is cheaper and more easily handled than liquid helium. They are less sensitive than conventional "low temperature" SQUIDs but good enough for many applications.
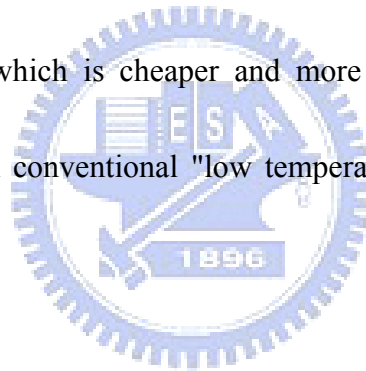
Multiferroic samples were measured at room temperature with a maximum magnetic field (H) 20 kO. The magnetization was measured every 250 Oe before H reached 1 kOe and measured every 300 Oe after 1 kOe. All the samples were under both in-plane and out-of-plane conditions. The in-plane measurement means the magnetic field is parable to the surface of the samples while the out-of-plane means the magnetic field is vertical to the surface of the samples.

3.2.4 FESEM

The first SEM image was obtained by Max Knoll, who in 1935 obtained an image of silicon steel showing electron channeling contrast [3]. The SEM was further developed by Professor Sir Charles Oatley and his postgraduate student Gary Stewart and was first marketed in 1965 by the Cambridge Instrument Company as the "Stereoscan". The first instrument was delivered to DuPont.

The FESEM is a type of electron microscope that images the sample surface by scanning it with a high-energy beam of electrons in a raster scan pattern. The electrons interact with the atoms that make up the sample producing signals that contain information about the sample's surface topography, composition and other properties such as electrical conductivity as shown in Fig 3-3.

We obtain the morphology of the three multiferroics by using field-emission scanning electron microscopy (FESEM).

Fig. 3-3 Picture of field-emission scanning electron microscopy (FESEM)

References

[1] V. M. Petrov, G. Srinivasan, and M. I. Bichurin et al., Phys. Rev. B **75**, 6 (2007).

[2] Range, Shannon K'doah. Gravity Probe B: Exploring Einstein's Universe with Gyroscopes. NASA*, **26** (2004).

[3] Knoll, Max, Zeitschrift für technische Physik **16,** 467 (1935).

[4] Von Ardenne, Manfred., Zeitschrift für Physik **108,** 553 (1938).

[5]Von Ardenne, Manfred, Zeitschrift für technische Physik **19**, 407 (1938).

[6] Von Ardenne M. Improvements in electron microscopes, GB patent 511204 (1937).

[7] Zheng H, Wang J, Lofland SE, Ma Z, Mohaddes-Ardabili L, Zhao T, Salamanca-Riba L, Shinde SR, Ogale SB, Bai F, Viehland D, Jia Y, Schlom DG, Wuttig M, Roytburd A and Ramesh R, Science **303**, 661 (2004).

Chapter 4 Results and Discussion

4.1 Results of X-ray Diffraction

4.1.1 Preference of *a*-Domain

The geometrical structure of disk-3 type was confirmed by using FESEM as Figure 4-1.
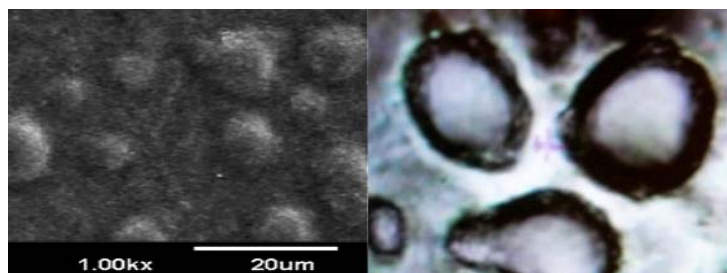
Fig. 4-1 The FESEM (left) and OM (right) images of disk-3 film.   The pictures reveal the average radius of disc is about 5 μm and the thickness is around 2 μm.   From the pictures above, we speculate that the film containts CFO discs in PTO matrix but not CFO rods in PTO matrix.

The XRD patterns taken at RT shown in Figure 4-2 reveal the correct phases in all multiferroics and "*" and "O" represent Si and Pt signals from the substrates, respectively. By using the refinement analysis of XRD data, the refined structure parameters were listed in Table 4-1.   The results of pure PTO powder agree with the JCPDS-International Center for Diffraction Data No. 78-0298.
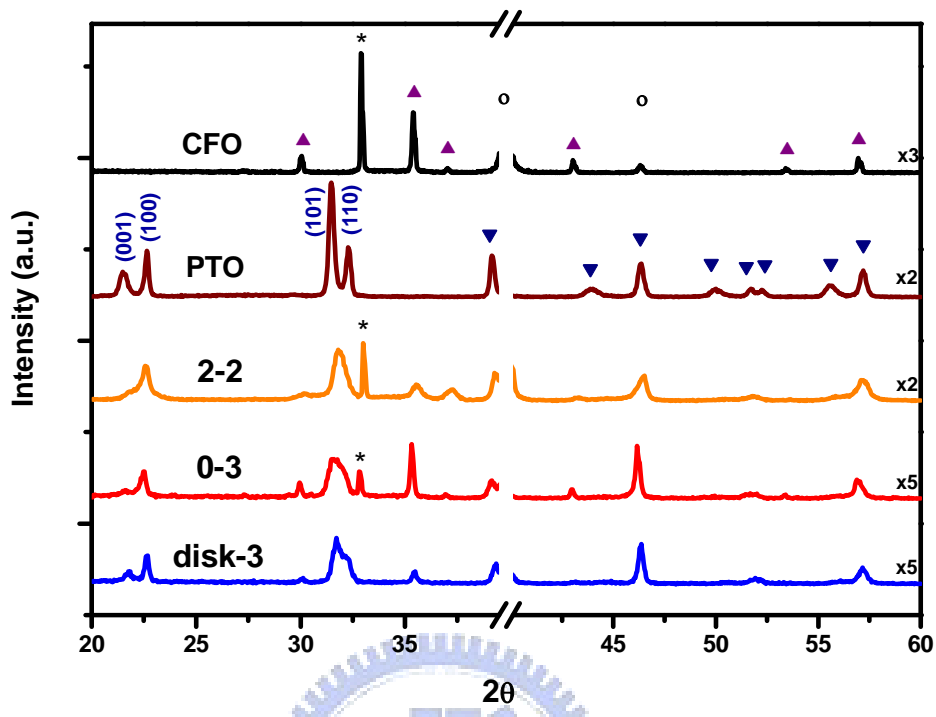
Fig. 4-2 X-ray diffraction pattern of the 2-2, 0-3, and disk-3 films: the curves labeled with CFO and PTO are both pure materials.

Table 4-1 The ferroelectric parameters of the films with different types

Films				PTO		
	$I_{(100)}/I_{(001)}$	a(Å)	Strain(%)	c(Å)	Strain(%)	c/a
Pure	1.98756	3.8616		4.0189		1.0407
2-2	3.692943	3.9078	1.1964	3.9422	-1.9085	1.0088
0-3	3.161934	3.8872	0.6629	3.9470	-1.7890	1.0120
disk-3	2.903217	3.8871	0.6604	3.9814	-0.9331	1.0269

According to Table 4-1, the intensity ratio of diffraction peaks (100) and (001) for pure PTO powder is close to 2, indicating the random orientation. The intensity ratios of diffraction peaks (100) and (001) for the disk-3, 0-3 and 2-2 types increase as compared with the pure PTO powder. It reveals that the PTO matrix in these samples prefers vertical *a*-axis growth with the *c*-axis lying on the substrate surface. Table 4-1 also shows that the *a*-axis of PTO matrix is lengthening with the compression of *c*-axis for the 2-2, 0-3, and disk-3 types. Because most PTO crystallites have their *c*-axes lying on the substrate surface along those of CFO ones, the tensile stress results from more than twice as many lattice constant of CFO as PTO one. Having larger lattice constant than PTO, CFO exerted strong tensile stress on the *a*-lattice of PTO and weak tensile stress on *c*-axis. The samples in which mostly *a*-axis directly connected with CFO was strongly elongated in *a*-axis that leads to compress the *c*-axis for preserving the unit cell volume. Consequently the lowering trend of *c*/*a* in Table 4-1 is not difficult to comprehend since the tensile stress induces *a*-lattice elongation resulting in the compressive *c*-axis.

From the intensity ratio of the diffraction peaks (100) and (001), the compression of *c*-axis should be most serious in disk-3 types and be less enhanced in the 2-2 types. On the contrary, we found the compression of *c*-axis is most serious in 2-2 types. The reason for this contradiction was that the XRD measurement is a macro result (covering mm^2 area). However, the ME coupling effect resulting from the elastic bonding at the interface is

transmitted through the stress between the interface of CFO and PTO matrix. The magnetic

properties in multiferrics would be also influenced by the stress, and it is more important to

observe the information of the interfacial strain which is sensitive to the behavior of

interfacial phonon.

4.2 Raman Spectra of PTO-CFO System

4.2.1 Analysis of Raman Spectra

The Raman spectra of pure PTO powders on substrates, namely PTO on Si (PTO/Si),

PTO on Pt precoated Si (PTO/Pt/Si), and three multiferroic films on Pt/Si substrates taken at

RT were plotted in figure 4-3. PTO belongs to the C_{4v}^1 (*P4mm*) space group with tetragonal

phase at RT [1], it has $3A_1$(TO), $3E$(TO), $3A_1$(LO), and $3E$(LO) Raman active modes. Figure

4-3 shows the phonon modes of PTO assigned according to Foster *et al* [2] to clarify the

structural variation of various types. A_1(TO) mode is especially interesting since the A_1(TO)

mode consists of displacements of Ti and oxygen ions relative to the lead ions and is, with the

E(1TO) mode, a soft mode. On the other hand, CFO belongs to O_h^7 (*Fd3*$\overline{m}$) space group

with cubic inverse spinel structure [3-5] and the Raman signal is hardly detected. Therefore,

we shall concentrate on change of Raman modes of PTO in various types of CFO/PTO
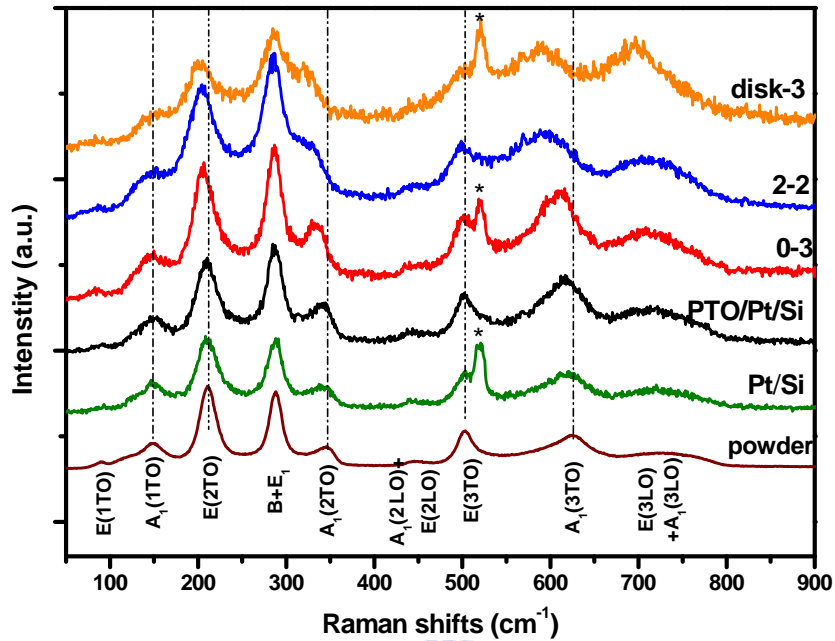
structures.

Fig. 4-3 Micro Raman spectra of disk-3, 2-2, 0-3 multiferroics together with those of PTO on Pt/Si, Si substrates, and PTO powder for comparison.

The phonon modes have remarkable shifts in their frequencies for different types, the A_1 modes especially. The A_1(1TO), A_1(2TO), and A_1(3TO) modes of PTO having frequencies at 150, 350, and 630 cm^{-1} show significantly red-shifted and broadened in all multiferroics as compared with the pure PTO powders, while the E modes vary just a little bit. We speculated that the reasons for the above-mentioned frequency shifts are not from structure change but from the strains either between structures and substrate or intra-structures. The significant shift of A_1 mode with invariable E mode in this study is unlike the lattice dynamics of Pb$_x$Sr$_{1-x}$TiO$_3$ polycrystalline powder reported by Kuo et al [6], in which the presence of substitution Sr^{2+} ions on PbTiO$_3$ yields structure changes so that shifts in all types of phonon modes.

In order to investigate the mechanism of strain, we need to recognize whether the shift of A_1 mode in multiferroics in this study is due to strains between substrate and structure or intra structures by referring to the spectra of PTO on Pt and Si substrates.   In Figure 4-2, we observed that all phonon modes of PTO on Pt and Si substrates are almost invariable as compared with ones of the pure PTO powder.   It indicates that shift of phonon mode of PTO in three multiferroic samples do not result from interaction between substrates and PTO but from the interfacial stress between CFO and PTO matrices.

4.2.2 Raman Shift and Coupling Mechanism

In order to further investigate the behavior of A_1 modes belonging to the PTO matrix in three multiferroic samples, the peak positions of $A_1(2TO)$ and $A_1(3TO)$ of various types were plotted in Figure 4-3.   The results of XRD indicate that PTO matrix favored c-axis to connect with CFO structures and the main interface of PTO to bond with CFO was (101) or (011).   The oxygen atoms and cations (Pb and Ti) of PTO oscillate along c axis in the $A_1(TO)$ modes, while the atoms oscillate on the plane composed by a and b axes in the E modes. Undoubtedly, the A_1 modes, describing the vibration of atoms along c direction, could be significantly influenced by the strains resulting from the interfacial mismatch of PTO with CFO.   However, owing to deficit of interaction with ferromagnetic materials, the behavior of E modes just like the pure PTO films having slightly shift in positions of their spectral peaks.

Further analyzing the phonon modes in three multiferroic samples by using peak fitting

method, we observed the largest shift of A_1(2TO) and A_1(3TO) in the disk-3 type, whereas the smallest shift in the 0-3 type as in Figure 4-4.　The magnitude of Raman shift in disk-3 disc type is also larger than that in 2-2 nanolayer type.　It indicates that the Raman shift in disk-3 type is due to the stronger coupling of two ferrite materials resulting from existing most a-domain [7-8], in which the c-axis of PTO matrix strongly bonds with CFO one, agreeing with the results of magnetic properties.　The magnetic property of multiferrics depends on the stress at the interface between $CoFe_2O_4$ and $PbTiO_3$ matrices, and the behavior of interfacial phonon is also sensitive to it.　We can confirm that micro-Raman measurement is a good probe into investigate the multiferrics.
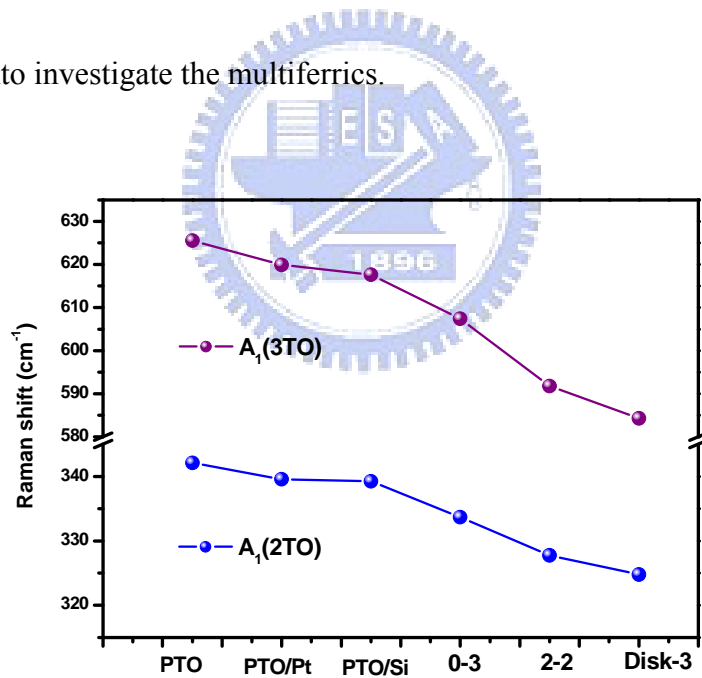

Fig. 4-4 The fitted Raman shift of the A_1(3TO) and A_1(2TO) modes as a function of film types.

4.3 Magnetic Properties Analysis

To investigate the stress dependence of behavior of interfacial phonon and ferromagnetic properties in multiferroics, the magnetic property was performed by SQUID as a probe of

lattice dynamics.

4.3.1 Nonsymmetrical Coercive Field

We measured the field dependent magnetizations at room temperature by applying

magnetic fields perpendicular or parallel to the surface of the films.　Figure 4-5 shows the

measured magnetic hysteresis loops for pure cobalt ferrite and different geometrical CFO

contained multiferroics.　The out-of-plane (Figure 4-5(a)) and in-plane (Figure 4-5(b)) loops

of the 0-3 type are similar to that of the pure CFO powder in the values of saturation

magnetization Ms and coercivity Hc.　The reason is that the 0-3 type sample was made of

dispersing pure CFO particles in PTO matrix and the chemical bonding between CFO and

PTO matrix may not form.
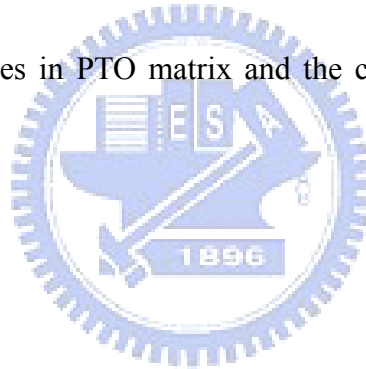
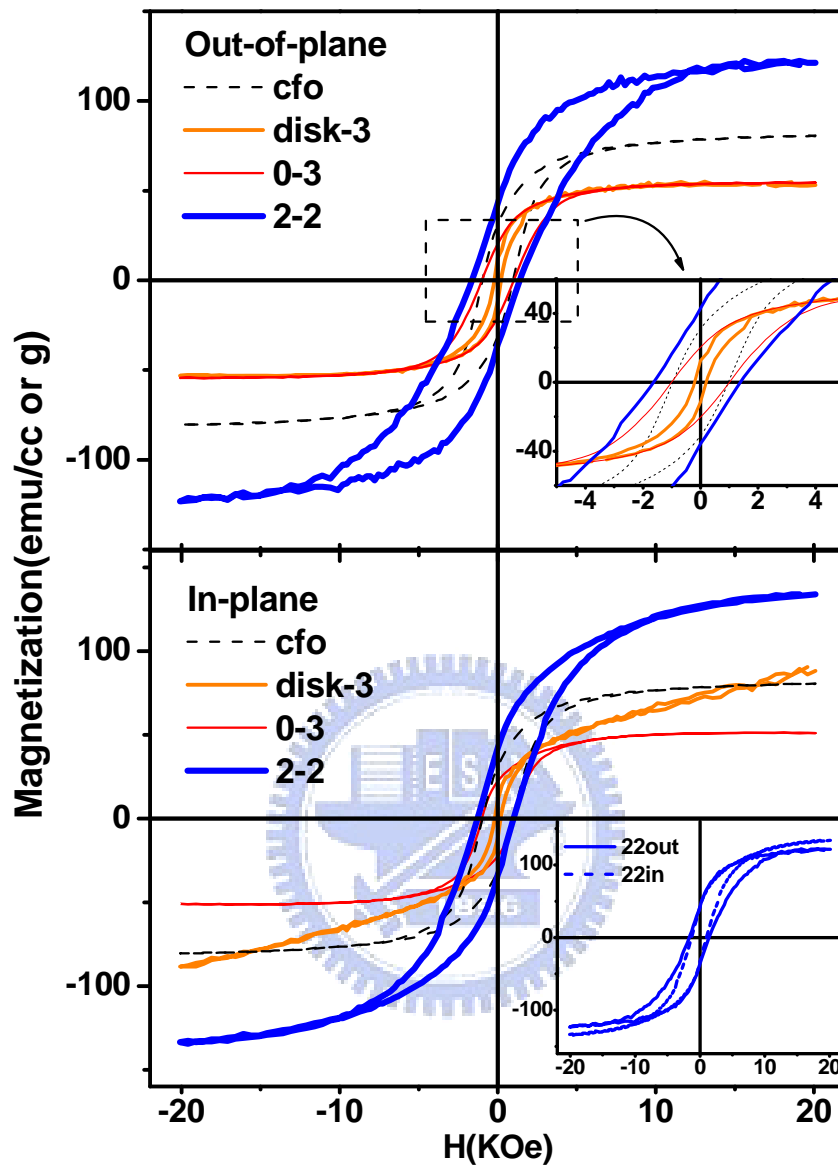Fig. 4-5 Out-of-plane (a) and in-plane (b) hysteresis loops for the pure CFO (diamond), 0-3 (star), 2-2 (square), and disk-3 (triangle) samples.

The out-of-plane coercivity Hc are about 0.97, 1.01, 1.51, and 0.2 kOe in pure cobalt

ferrite powder, 0-3, 2-2, and disk-3 types, respectively. Notice that the out-of-plane

coercivity Hc of the disk-3 type is only 0.2 kOe, which is much lower than those of other

samples. The easier magnetization characteristic should contribute to the increase of the total magnetocrystalline anisotropy energy related to the magnetoelastic coupling due to the compressive stress in the CFO phase caused by the lattice mismatch between the CFO and PTO matrices[15] as observed in our Raman results. Zhang *et al.* [9] also considered the reason that the lattice mismatch induces strains can indeed alter the magnetic properties.

The lower insets of Figure 4-5 shows the hysteresis loops of the 2-2 type measured in-plane and out-of-plane with an external field up to 20 kOe. It reveals that the out-of-plane coercivity Hc is larger than the in-plane one with nonsymmetrical values for the negative and the positive magnetic field. The differences in Hc reveal that it is harder to rotate the magnetic domain in vertical direction than in horizontal direction. It should contribute to the increase of the total magnetocrystalline anisotropy energy related to the magnetoelastic coupling due to the compressive stress in the CFO phase caused by the lattice mismatch between the CFO and PTO matrix [10]. Phenomena which the loop slightly shifted toward negative magnetic field may come from magnetoelectric effect between ferroelectric and ferromagnetic film. The more obvious trend of the result of the disk-3 type was observed. The in-plane negative and the positive coercive field Hc of 2-2 type are about -1287.62 and 949.09 Oe, as these of disk-3 type are -187.74 and 123.64 Oe. The difference between the negative and the positive coercive field Hc of disk-3 type is 34.14%, which is larger than that of 2-2 type (26.37%).

4.3.2 Magnetic Anisotropy

The absence of saturation magnetization Ms is observed in both the out-of-plane and in-plane loops of disk-3 and 2-2 types. We speculate that the absence of saturation magnetization Ms may be due to the coupled interaction between ferromagnetic and ferroelectric materials. Under the magnetization process, the change of CFO structure resulting from magnetostriction would produce stress on the surrounding PTO structure. As the magnetic field increases, the strain imposed by CFO matrix on PTO one will increase. The strained PTO bonding along the interface would eventually affect the boundary structure of CFO matrix. Consequently, the larger the nonsymmetrical values of coercivity Hc, the more difficult to saturate magnetization of CFO is found in the disk-3 type than the others, since the disk-3 type has the largest stress due to the lattice misfit and the strongest chemical bonding between the CFO and PTO matrix.

4.4 Summary

The characteristics of three different geometric forms of the $PbTiO_3$-$CoFe_2O_4$ multiferroics fabricated by the simple solution method has been investigated using OM, FESEM, XRD, SQUID, and Raman spectroscopy. The analysis of the magnetic and Raman measurements under different geometric forms indicates the dependence of magnetic property and interfacial phonon behavior on stress/strain due to the lattice misfit and the strongest

chemical bonding at the interface between $CoFe_2O_4$ and $PbTiO_3$ matrices. The larger the

nonsymmetrical values of coercivity Hc and the absence of saturation magnetization Ms of

$CoFe_2O_4$ consist with the largest shift of A_1(2TO) and A_1(3TO) modes of $PbTiO_3$ in the disk-3

type than the other structures of the CFO and PTO multilayered structure and the CFO

particles embedded in PTO matrix.

References

[1] J. A. Sanjurjo, E. L ez-Cruz, and Gerald Burns, Phys. Rev. B **28** (12), 7260 (1983).

[2] C. M. Foster, Z. Li, M. Grimsditch, S. K. Chan, and D. J. Lam, Phys. Rev.B **48**, 10160 (1993).

[3] Zhongwu Wang, R. T. Downs, V. Pischedda et al., Phys. Rev. B **68**, 094101 (2003).

[4] O. N. Shebanova and P. Lazor, J. Solid State Chem. **174**, 424 (2003).

[5] J. Larry Verble, Phys. Rev. B **9**, 5236 (1974).

[6] S. Y. Kuo, W. Y. Liao, and W. F. Hsieh, Phys. Rev. B **64**, 224103 (2001).

[7] S. H. Lee, H. M. Jang, S. M. Cho, and Gyu-Chul Yi, Appl. Phys. Lett. **80**, 3165 (2002).

[8] A. Bartasyte, O. Chaix-Pluchery, J. Kreisel, C. Jimenez, F. Weiss, A. Abrutis, Z. Saltyte, and M. Boudard J. Appl. Phys. **103**, 8 (2008).

[9] Y. Zhang, C. Deng, J. Ma, Y. Lin, and C. W. Nan, Appl. Phys. Lett. **92**, 062911 (2008)

[10] R. C. O'Handley, "Modern Magnetic Materials: Principles and Applications," (Wiley, New York, 2000).

Chapter 5 Conclusion and future works

5.1 Conclusion

The main intentions of this work were the study of interfacial interaction between the ferroelectric $PbTiO_3$ and ferromagnetic $CoFe_2O_4$ in the micro region of the multiferroic system by using micro Raman spectroscopy and its influence on the ferromagnetic properties in multiferroic systems by using SQUID technique. All the results and conclusion are summarized as below:

We used chemical solution method and spin-coating technique to fabricate the three different geometrical of multiferroics which were respectively the 0-3 type meaning the particular $CoFe_2O_4$ particular embedded in the $PbTiO_3$ matrix, the 2-2 type combining the $CoFe_2O_4$ and the $PbTiO_3$ multilayer structure, and the disk $CoFe_2O_4$ aligned in $PbTiO_3$ matrix named disk-3 type. The XRD showed the preferred a-domain with the c-axis of $PbTiO_3$ lining in-plane and decrease of the tetragonality in all three multiferroic thin films. On the other hand, the energy of $A_1(2TO)$ and $A_1(3TO)$ modes of all types showed red-shifting in Raman spectrum as they vibrated along the c-axis in which the $PbTiO_3$ bonded with the $CoFe_2O_4$ strongly. Finally, in the magnetic hysteresis loop, we observed the lower coercive field (Hc), the more nonsymmetrical coercive field ($\triangle$Hc%), and the harder saturated saturation magnetization (Ms) in disk-3 type than in other type multiferroics, which were well agreed with the more shifting of phonon modes in Raman spectrum.

5.2 Perspective

Multiferroic materials are nowadays of high interest for its electric-magnetic dual properties. There are still many works need to be accomplished in the future to realize the conversion between magnetic energy and electric energy.

In the previous works, we successfully demonstrated the three architecture multiferroics, however the optimal temperatures for different types to exhibit stable chemical compositions, strong interfacial bonding, and hence the effective stress-mediated ME process still need to be ascertained. Cathodoluminescence (CL) image is a suitable tool to analyze the crystal defects and local impurities distribution. This is because the energy gap and intensity of CL signals will change when the defects and impurity exist in materials. Therefore CL provides a direct measurement of interface chemistry and strucure images for multiphase multiferroics.

Among all the multiferroics, disk-3 type is of specious interest since it holds great ME effect for applications. But how to increase its interface between pervoskite and spinel structure remains a challenge. We proposed two methods to reduce the sizes of CFO disks. First, by reducing the annealing temperatures to prevent the growth of CFO grains, one can get the rod-shaped cobalt ferrites rather than disc forms. Second, we can synthesize 1-3 multiferroic with rod-shaped PTO fabricated first by molten salt methods, and the controllable sizes and densities of rods could be derived which promises to decrease leakage current problem.

We have shown that the static Raman spectrum is an important parameter for studying the local elastic interaction between pervoskite and spinel structures. Furthermore, magnetoelectricity is a dynamic process of exchanges between polar and spin subsystems under application of magnetic field or electric field, so that the magnetic/electric field dependent phonon dynamics is an interesting topic for future investigation. On the other hand, theoretical calculations on Raman spectra of multiphase multiferroics are significant but still lacking. The correlation between ME effect and Raman shift should be verified by both measuring the magnetoelectricity coefficient and first principal calculations.